Supporting Information for

# Tuning the Redox Properties of Fullerene Clusters within a Metal-Organic Capsule

Felix J. Rizzuto[‡], Daniel M. Wood[‡], Tanya K. Ronson, Jonathan R. Nitschke

## Table of Contents

# 1. Materials and methods

All reagents and solvents were purchased from commercial sources and used as supplied unless otherwise stated. $Fe(BF)_4 \cdot 6(H_2O)$ was purchased from Sigma Aldrich. Deuterated solvents were purchased from Euriso-Top (C. E. Saclay) or Sigma Aldrich. The synthesis and characterization of the triflate salt of **1** and its $Ni^{II}$-4,4'-(2,8,12,18-tetraethyl-3,7,13,17-tetramethylporphyrin-5,15-diyl)dianiline subcomponent (**Ni-NH$_2$**) have been reported elsewhere.[1]

## 1.1 Nuclear Magnetic Resonance (NMR)

NMR spectra were recorded using Bruker Avance DPX 400 MHz and 500 MHz TCI cryoprobe spectrometers. Chemical shifts for $^1$H, $^{13}$C and $^{19}$F are reported in ppm on the $\delta$ scale; $^1$H and $^{13}$C were referenced to the residual solvent peak and $^{19}$F was referenced to an internal standard of $C_6F_6$ in $CD_3CN$ at −164.9 ppm. Coupling constants ($J$) are reported in hertz (Hz). The following abbreviations are used to describe signal multiplicity for $^1$H, $^{13}$C and $^{19}$F NMR spectra: s: singlet, d: doublet, t: triplet, dd: doublet of doublets; dt: doublet of triplets; m: multiplet, br: broad.

DOSY NMR experiments were performed on a Bruker 500 MHz NMR spectrometer. Maximum gradient strength was 6.57 G/cm A. The standard Bruker pulse program, ledbpgp2s, employing a stimulated echo and longitudinal eddy-current delay (LED) using bipolar gradient pulses for diffusion using 2 spoil gradients was utilized. Rectangular gradients were used with a total duration of 1.5 ms. Gradient recovery delays were 875-1400 μs. Individual rows of the S4 quasi-2D diffusion databases were phased and baseline corrected.

## 1.2 Mass spectrometry (MS)

Low resolution electrospray ionisation (LR-ESI) mass spectrometry was undertaken on a Micromass Quattro LC mass spectrometer (cone voltage 10-30 eV; desolvation temp. 313 K; ionization temp. 313 K) infused from a Harvard syringe pump at a rate of 10 μL min$^{-1}$. High resolution electrospray ionisation mass spectrometry (HRMS-ESI) was performed on a

Waters LCT Premier Orbitrap Mass Spectrometer featuring a Z spray source with electrospray ionisation and modular LockSpray interface. Mass spectrometry samples for $(C_{60})_{1\text{-}3}\subset$**1** generated in $MeNO_2$ and $(C_{60})_{1\text{-}4}\subset$**1** generated in $PhNO_2$ were both dissolved in $CH_3CN$ for collection. Samples of $(C_{60})_{1\text{-}4}\subset$**1** formed in $PhNO_2$ showed no sign of redistribution to the 1-3 adduct after 8 hours standing at RT in $CH_3CN$. This indicates stability of the respective host-guest occupancies over the course of the electrochemical and spectroscopic experiments (see below).

### 1.3 UV-Vis spectroscopy

UV-Visible absorption spectroscopy was performed using a Perkin Elmer Lambda 750 UV-Vis-NIR spectrophotometer fitted with a PTP-1 Peltier temperature controller accessory. Spectra were obtained in double beam mode using only the (front) analyte beam to record spectra, with air in the (rear) reference path. A background spectrum of the neat solvent was recorded using the analyte beam prior to each experiment and baseline correction applied using the Perkin Elmer WinLab software suite. Samples were analysed using quartz cuvettes with optical path lengths of 10 mm.

*Procedure for UV-Vis titration:* A solution of host ($5.65 \times 10^{-6}$ M) in $PhNO_2$ (2.00 mL) in a UV-Vis cuvette was titrated with a solution of the same concentration of host ($5.65 \times 10^{-6}$ M) and excess $C_{60}$ guest ($6.24 \times 10^{-4}$ M) in $PhNO_2$, such that the concentration of the host remained constant with each addition of guest. Upon each addition, the solution was manually stirred for 2 min before acquiring the UV-Vis spectrum.

Fullerenes absorb strongly in the visible region. To counter the absorption of free fullerenes during the titration, a 'blank' titration was conducted with a solution of guest ($6.24 \times 10^{-4}$ M) in $PhNO_2$ into a UV-Vis cuvette with $PhNO_2$ (2.00 mL). This enabled the absorption spectra of the free fullerene to be subtracted from the original titration data. The validity of this method was supported by the presence of stable isosbestic points after subtraction of the individual fullerene spectra, furthermore indicating stability of the complex over the course of the titration.

Binding isotherms for the titrations were calculated using BINDFIT.[2] As $PhNO_2$ displays strong absorption >450 nm, only the two Q bands could be used in the fitting processes. The

equations used for these analyses are available in the review by Thordarson.[3] The covariance of the fit (variance of the residuals divided by the variance in the data), along with the appearance of fitting residuals and error values, were used to qualify the appropriateness of each model, following the methods outlined by Thordarson and others.[4]

### 1.4 Cyclic voltammetry

Solution state cyclic voltammetry (CV) was performed using a BioLogic SP-150 potentiostat with ferrocene (Fc) as an internal reference. Measurements were conducted under an Ar atmosphere using a conventional three-electrode cell: a glassy carbon working electrode, a Pt wire auxiliary electrode, and a $Ag/Ag^+$ quasi-reference electrode. A 0.1 M $n$$Bu_4NPF_6$/$CH_2Cl_2$, /$CH_3CN$ or /(1:4 DMF:$CH_3CN$) electrolyte was used, with scan rates in the range 25-1000 mV $s^{-1}$. The $^1H$ NMR spectrum of $C_{60}$⊂**2** in a 1:4 $d_7$-DMF:$CD_3CN$ solution indicated stability in this solvent mixture over the course of the electrochemical experiment.

## 2. X-ray crystallography

Data were collected at Beamline I19 of Diamond Light Source[5] employing silicon double crystal monochromated synchrotron radiation (0.6889 Å) with ω scans at 100(2) K. Data integration and reduction were undertaken with SAINT and XPREP[6] or CrysalisPro.[7] Subsequent computations were carried out using the WinGX-32 graphical user interface.[8] Multi-scan empirical absorption corrections were applied to the data using SADABS.[6] Structures were solved by direct methods using SHELXT-2013[9] or SUPERFLIP[10] then refined and extended with SHELXL-2013.[9] In general, non-hydrogen atoms with occupancies greater than 0.5 were refined anisotropically. Carbon-bound hydrogen atoms were included in idealised positions and refined using a riding model. Disorder was modelled using standard crystallographic methods including constraints, restraints and rigid bodies where necessary. Crystallographic data along with specific details pertaining to the refinement follow. Crystallographic data have been deposited with the CCDC (1549079 and 1549080). The crystal structures of **1** and **Ni-NH$_2$** have been reported elsewhere[1] and can be accessed via the CCDC (1038794 and 1038795, respectively).

### 2.1 Crystal structure of $(C_{60})_3\subset$**1·8OTf·0.5Et$_2$O**

Formula $C_{526}H_{317}F_{24}Fe_4N_{48}Ni_6O_{24.50}S_8$, $M$ 8989.40, triclinic, space group P–1 (#2), $a$ 31.3706(16), $b$ 31.5616(16), $c$ 33.5735(15) Å, $\alpha$ 65.910(2), $\beta$ 67.466(2), $\gamma$ 62.464(3)º, $V$ 26120(2) Å$^3$, $D_c$ 1.143 g cm$^{-3}$, $Z$ 2, crystal size 0.030 by 0.020 by 0.010 mm, colour dark brown, habit block, temperature 100(2) Kelvin, $\lambda$(synchrotron) 0.6889 Å, $\mu$(synchrotron) 0.353 mm$^{-1}$, $T$(SADABS)$_{min,max}$ 0.5082, 0.7442, 2$\theta_{max}$ 33.36, $hkl$ range –25 26, –26 25, –27 27, $N$ 91331, $N_{ind}$ 31517, $R_{merge}$ 0.1065, $N_{obs}$ 14141(I > 2σ(I)), $N_{var}$ 3802, residuals* $R1(F)$ 0.1310, $wR2(F^2)$ 0.3751, GoF(all) 1.126, $\Delta\rho_{min,max}$ –0.486, 0.697 e$^-$ Å$^{-3}$.

*$R1 = \Sigma||F_o| - |F_c||/\Sigma|F_o|$ for $F_o > 2\sigma(F_o)$; $wR2 = (\Sigma w(F_o^2 - F_c^2)^2/\Sigma (wF_c^2)^2)^{1/2}$ all reflections $w=1/[\sigma^2(F_o^2)+(0.2000P)^2 +750.0000P]$ where $P=(F_o^2+2F_c^2)/3$

*Specific refinement details*

X-ray quality crystals of $(C_{60})_3\subset$**1**$\cdot 8OTf\cdot 0.5Et_2O$ were grown by vapor diffusion of diethyl ether into an acetonitrile solution of the $OTf^-$ salt of $(C_{60})_{1\text{-}3}\subset$**1**. The crystals employed in this study proved to be weakly diffracting and rapidly suffered solvent loss. Rapid (<1 min) handling prior to flash cooling in the cryostream was required to collect data. Despite these measures and the use of synchrotron radiation few reflections at greater than 1.2 Å resolution were observed. Despite these limitations the data is more than sufficient to establish the connectivity of the structure. The asymmetric unit contains one complete $Fe_4L_6$ tetrahedron and three $C_{60}$ guests. There is a significant amount of thermal motion in the extremities of the molecule and extensive thermal parameter and bond length restraints were required to facilitate realistic modelling of the organic parts of the structure. The bond lengths and angles within pairs of porphyrin groups were restrained to be similar to each other and all phenyl and pyridyl rings were modelled as rigid groups.

Reflecting the instability of the sample, there is a very high level of disorder within the structure. One iron(II) center and associated pyridyl-imine ligands were modelled as disordered over two positions with occupancies of 0.65089/0.34911. One porphyrin group was modelled as disordered over three positions with occupancies of 0.45/0.30/0.25. Some ethyl and methyl substituents on the minor occupancy position were not included in the model. All disordered groups were refined with isotropic thermal parameters.

The positioning of the three $C_{60}$ molecules was established unequivocally from the electron density map. Each $C_{60}$ molecule is completely spherically disordered and behaves as a shell of electron density, similar to disorder seen in other fullerene structures.[11-13] To facilitate realistic modelling of the fullerenes a rigid-body constraint of a well-defined $C_{60}$ was used and each $C_{60}$ was modelled as disordered over two locations with isotropic thermal parameters.

Only three triflate lattice sites (per tetrahedron) could be located. Two of these triflate anions were modelled as disordered over two locations (and with overall partial occupancy) with a number of bond length and thermal parameter restraints. The remaining anions (5.7 per tetrahedron) and solvent molecules within the lattice were significantly disordered and despite numerous attempts at modelling, including with rigid bodies, no satisfactory model for the electron-density associated with them could be found. Therefore, the SQUEEZE[14]

function of PLATON[15] was employed to remove the contribution of the electron density associated with the anions and disordered solvent from the model, which resulted in more satisfactory residuals.

### 2.2 Crystal structure of $C_{60}\subset$**1**$\cdot 8BF_4\cdot 6.5PhNO_2$

Formula $C_{435}H_{344.50}B_8F_{32}Fe_4N_{54.50}Ni_6O_{13}$, *M* 7813.27, Trigonal, space group R–3 (#167), *a* 38.8188(8), *b* 38.8188(8), *c* 111.372(3) Å, $\gamma$ 120º, *V* 145342(7) Å$^3$, $D_c$ 1.071 g cm$^{-3}$, *Z* 12, crystal size 0.015 by 0.010 by 0.010 mm, colour dark brown, habit block, temperature 100(2) Kelvin, $\lambda$(Synchrotron) 0.6889 Å, $\mu$(Synchrotron) 0.377 mm$^{-1}$, $T(\text{SADABS})_{min,max}$ 0.5653, 0.7441, $2\theta_{max}$ 33.36, *hkl* range –32 32, –32 32, –92 92, *N* 316681, $N_{ind}$ 9789($R_{merge}$ 0.0856), $N_{obs}$ 8028(I > 2σ(I)), $N_{var}$ 1302, residuals* *R*1(*F*) 0.1424, *wR*2($F^2$) 0.3879, GoF(all) 1.148, $\Delta\rho_{min,max}$ –0.397, 0.658 e$^-$ Å$^{-3}$.

*$R1 = \Sigma||F_o| - |F_c||/\Sigma|F_o|$ for $F_o > 2\sigma(F_o)$; $wR2 = (\Sigma w(F_o^2 - F_c^2)^2/\Sigma(wF_c^2)^2)^{1/2}$ all reflections
$w=1/[\sigma^2(F_o^2)+(0.2000P)^2+1500.0000P]$ where $P=(F_o^2+2F_c^2)/3$

*Specific refinement details*

X-ray quality crystals of $C_{60}\subset$**1**$\cdot 8BF_4\cdot 6.5PhNO_2$ were grown by vapor diffusion of diethyl ether into a nitrobenzene solution of $(C_{60})_{1\text{-}4}\subset$**1**. The crystals employed in this study proved to be weakly diffracting and rapidly suffered solvent loss. Rapid (<1 min) handling prior to flash cooling in the cryostream was required to collect data. Despite these measures and the use of synchrotron radiation few reflections at greater than 1.2 Å resolution were observed. Despite these limitations the data is more than sufficient to establish the connectivity of the structure. The asymmetric unit contains one third of a $Fe_4L_6$ tetrahedron and $C_{60}$ guest. There is a significant amount of thermal motion in the extremities of the molecule and extensive thermal parameter and bond length restraints were required to facilitate realistic modelling of the organic parts of the structure. The bond lengths and angles within the two crystallographically unique organic ligands were restrained to be similar to each other and some additional bond length restraints were applied to achieve a reasonable model.

Three of the porphyrin ethyl substituents were modelled as disordered over two locations and several more show evidence of thermal motion resulting from the presence of dynamic disorder in these groups. Consequently, there are a number of close contacts between symmetry-generated and/or disordered methyl groups. One nitrobenzene solvent molecule was modelled as disordered over two locations and all nitrobenzenes were modelled with isotropic thermal parameters and substantial bond length restraints.

The positioning of the $C_{60}$ molecule was established unequivocally from the electron density map. This $C_{60}$ molecule is rotationally disordered around a threefold axis and behaves as a shell of electron density, similar to disorder seen in other fullerene structures.[11-13] To facilitate realistic modelling a rigid-body constraint of a well-defined $C_{60}$ was used and the $C_{60}$ was refined with isotropic thermal parameters. The thermal parameters of the $C_{60}$ atoms remain higher than ideal, possibly indicative of further unresolved disorder.

Only one tetrafluoroborate lattice site (per asymmetric unit) could be located. This tetrafluoroborate anion was modelled as disordered over three locations with a number of bond length and thermal parameter restraints. The remaining anions (five per tetrahedron) and additional solvent molecules within the lattice were significantly disordered and despite numerous attempts at modelling, including with rigid bodies, no satisfactory model for the electron-density associated with them could be found. Therefore, the SQUEEZE[14] function of PLATON[15] was employed to remove the contribution of the electron density associated with the anions and disordered solvent from the model, which resulted in more satisfactory residuals.

## 3. Synthesis and characterisation of **1**$(BF_4)_8$

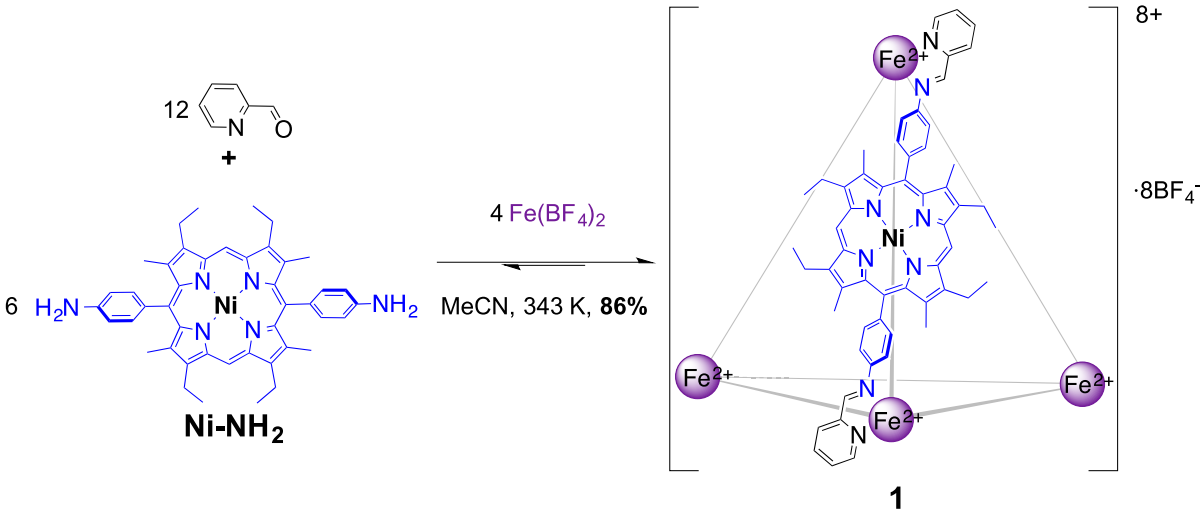


**Ni-NH$_2$** (39.6 mg, 54.9 μmol, 6 equiv), $Fe(BF_4)_2 \cdot 6H_2O$ (13.0 mg, 38.5 μmol, 4 equiv) and 2-formylpyridine (10.7 μL, 112.5 μmol, 12 equiv) were combined in MeCN (10 mL) and sonicated. The mixture was heated at 343 K for 6 h under $N_2$. The resultant purple solution was filtered through Celite, frozen, then $Et_2O$ (40 mL) was layered on top and the mixture was left at 298 K for 12 h, allowing crystals to form. The resultant solid was isolated by filtration, washed with additional $Et_2O$, then dried to give a purple solid (49.5 mg, 7.9 μmol, 86 %).

$^1$H NMR (400 MHz, 298 K, $CD_3CN$): $\delta$ 9.66 – 9.25 (m, 24H), 8.77 (dd, $J$ = 16.3, 7.6 Hz, 12H), 8.54 (d, $J$ = 7.1 Hz, 12H), 8.12 – 7.53 (br, m, 48H), 6.67 (br, 24H), 3.71 (m, br, 48H), 2.54 – 2.00 (m, br, 72H), 1.61 – 1.28 (m, 72H) ppm. See Figure S1 for assignments.

$^{13}$C NMR (125 MHz, 298 K, $CD_3CN$): $\delta$ 176.4, 159.7, 157.3, 152.2, 147.0, 143.1, 141.1, 140.7, 139.6, 138.9, 135.1, 132.4, 131.5, 122.0, 116.3, 97.2, 20.0, 17.7, 17.6, 16.5 ppm.

$^{19}$F NMR (376 MHz, 298 K, $CD_3CN$) δ –151.7 (s, free $BF_4^-$) ppm.

LR-ESI-MS [charge, calculated for $Fe_4(C_{56}H_{52}N_8Ni)_6(BF_4)_{(8-x)}(F)_x$]: $m/z$ = 938.6 [**1**$(F)_2^{6+}$, 938.9], 802.1 [**1**$(F)^{7+}$, 802.4], 699.8 [**1**$^{8+}$, 699.7].

HR-ESI-MS: calculated for **1**$(F)^{7+}$ $m/z$ = 802.4201, found 802.4183.

Elemental analysis: calcd (%) for $Fe_4(C_{56}H_{52}N_8Ni)_6(BF_4)_8 \cdot 14.8H_2O$ = C 62.08, H 5.17, N 10.10, found: C 61.82, H 4.90, N 10.28.

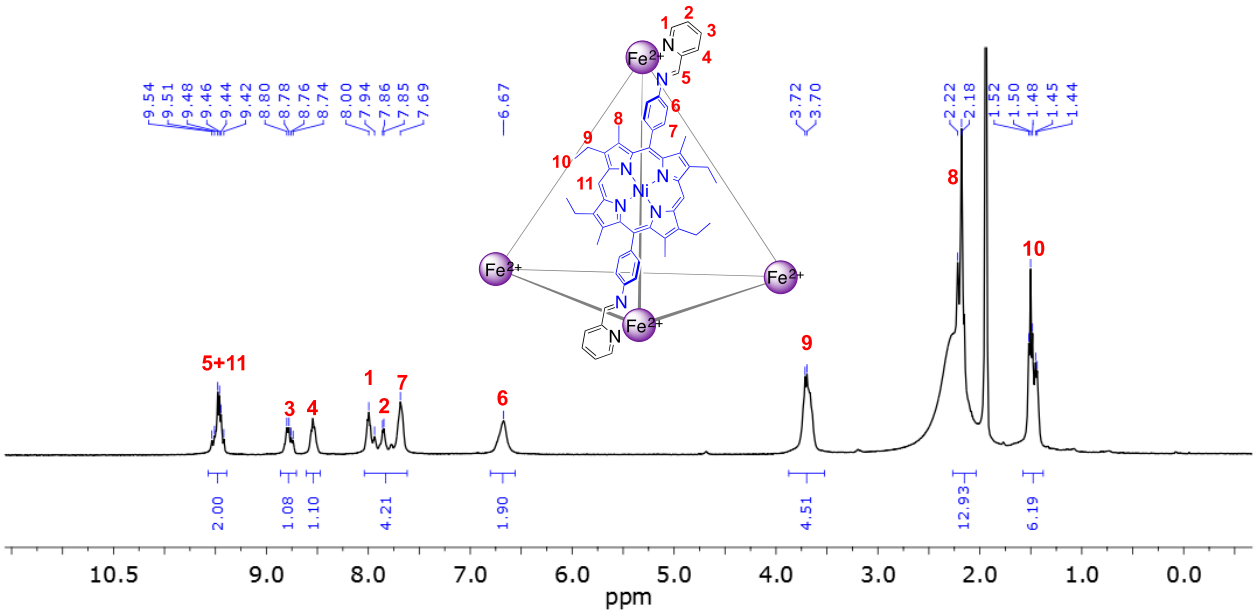


**Figure S1.** $^{1}$H NMR spectrum (400 MHz, 298 K, $CD_3CN$) of **1**$(BF_4)_8$.

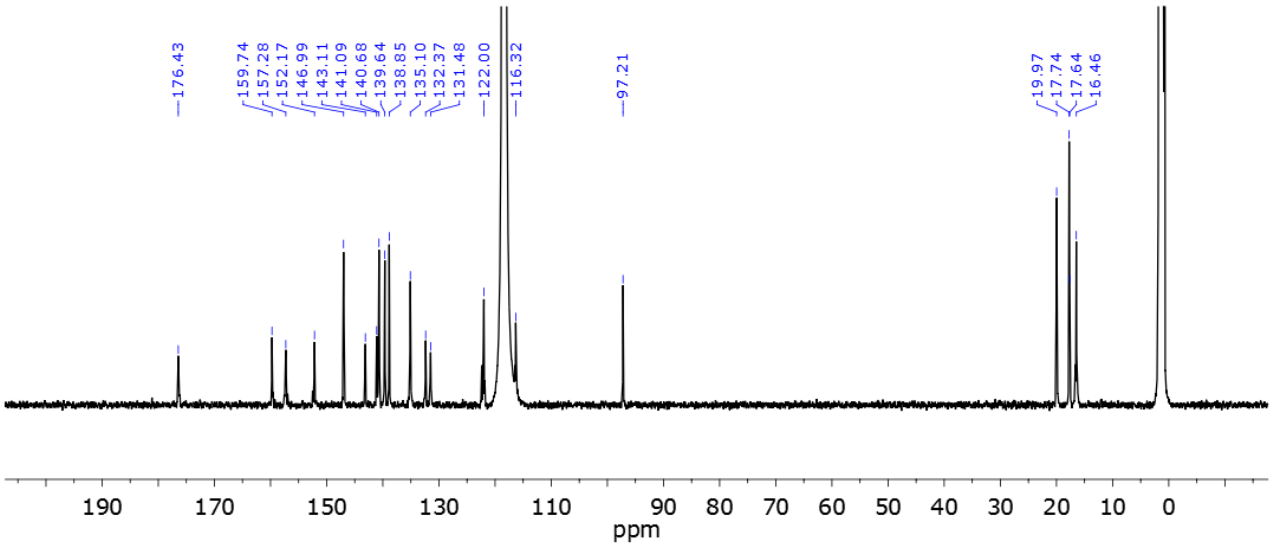


**Figure S2.** $^{13}$C NMR spectrum (125 MHz, 298 K, $CD_3CN$) of **1**$(BF_4)_8$.

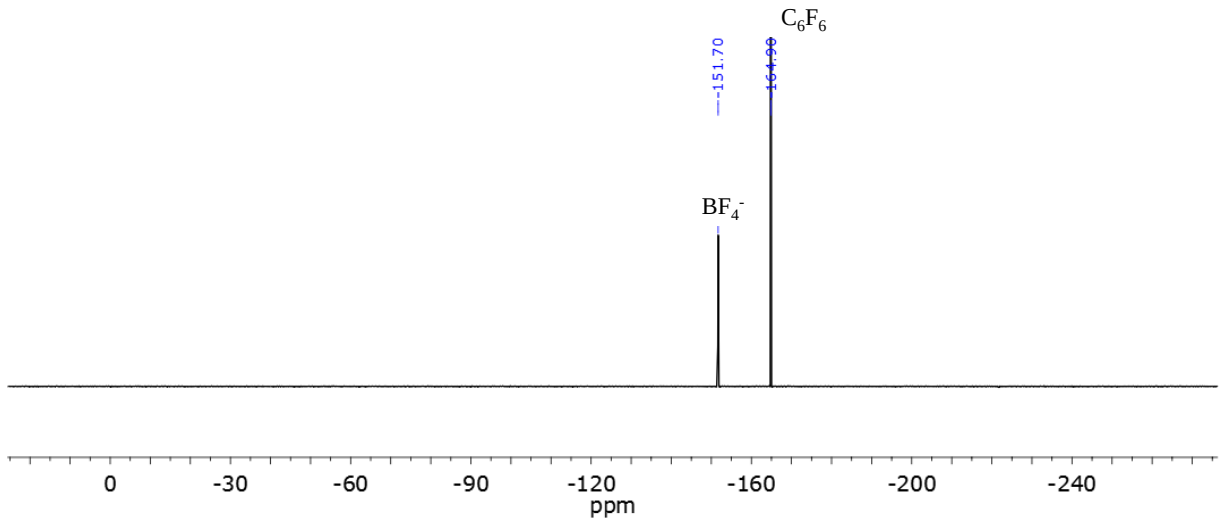


**Figure S3.** $^{19}$F NMR spectrum (375 MHz, $CD_3CN$) of **1**$(BF_4)_8$.

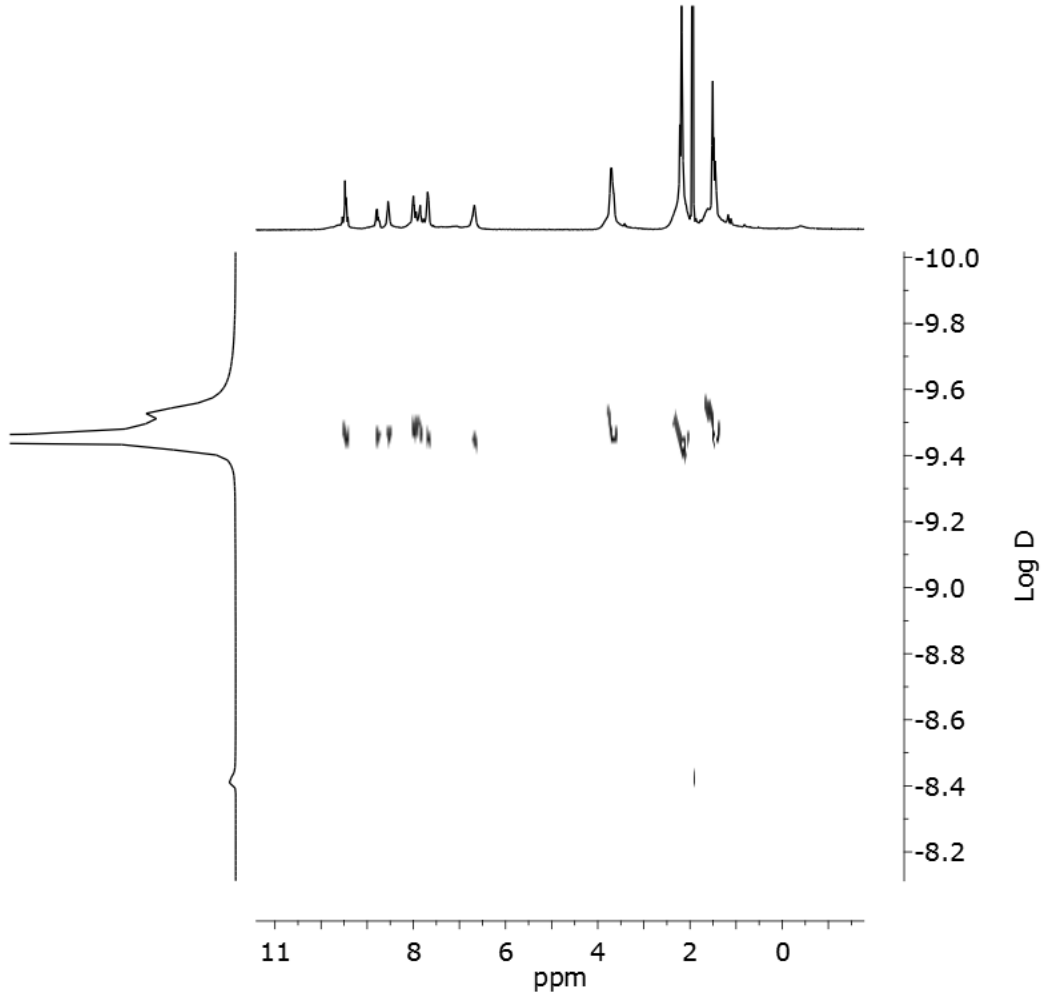


**Figure S4.** $^1$H-DOSY spectrum (400 MHz, 298 K, $CD_3CN$) spectrum of **1**$(BF_4)_8$.

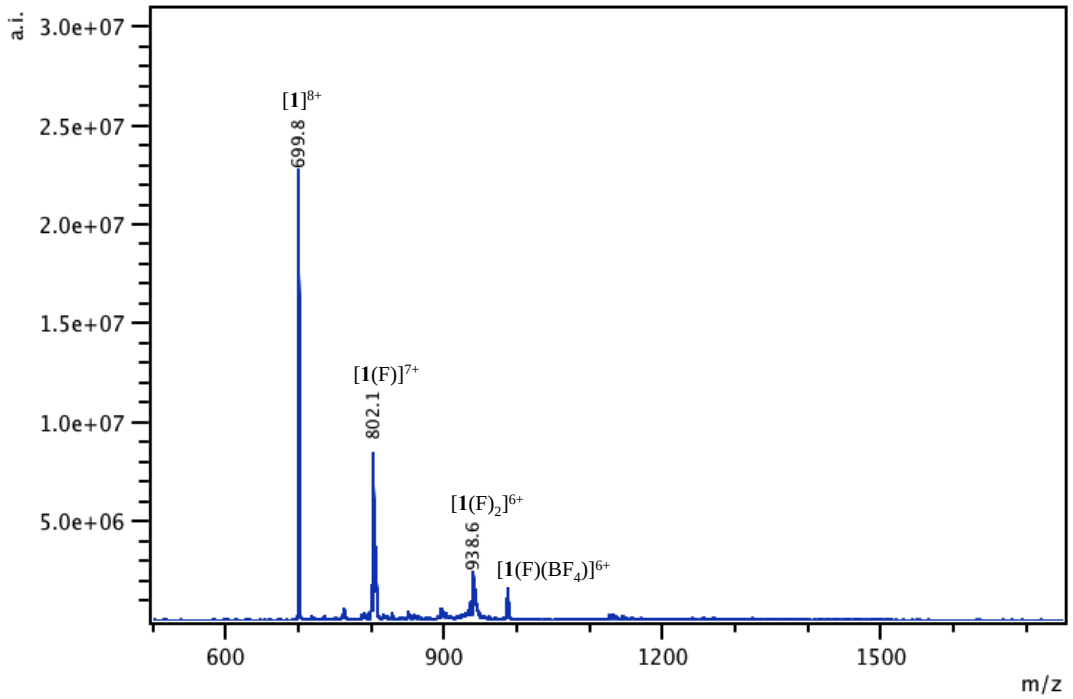


**Figure S5.** Low resolution ESI-MS spectrum of **1**. $F^-$ was observed to serve as counterion in ESI-MS experiments. The $^{19}F$ NMR spectrum of **1** contained only signals for uncoordinated $BF_4^-$, with no signal observed for $F^-$. From these observations, it was concluded that the fluoride observed by ESI-MS represents a minor impurity in solution, present as an impurity in the metal salt used in the synthesis of **1**.

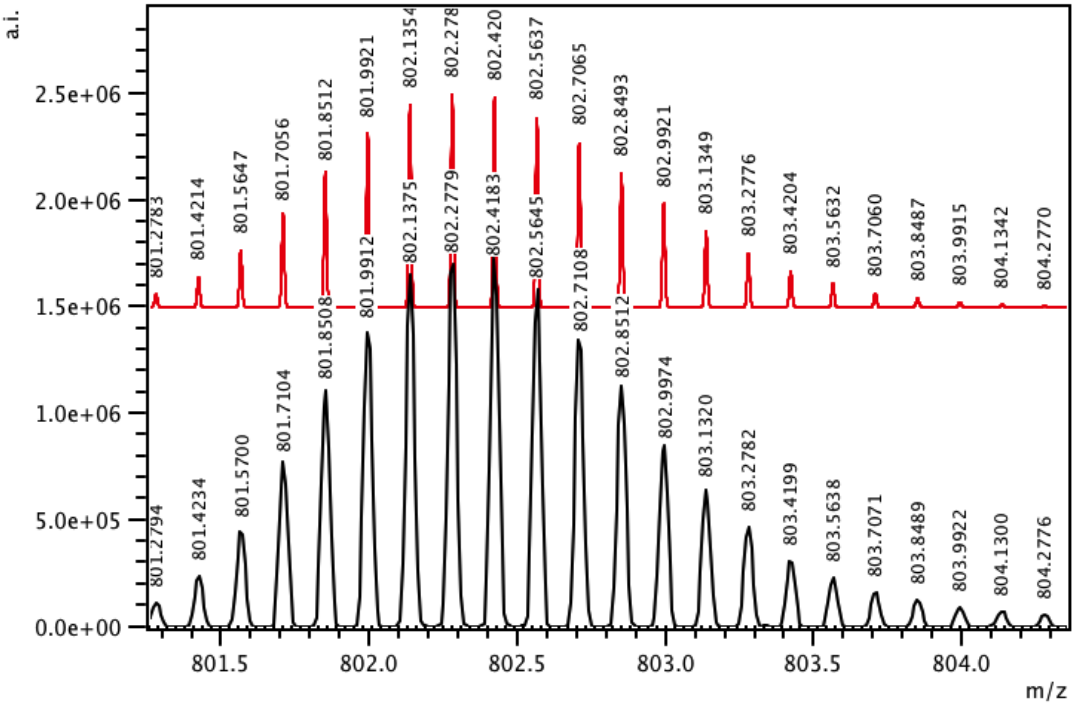


**Figure S6.** High resolution ESI mass spectrum of **1**$(BF_4)_8$, showing the theoretical isotope model (top) and the observed data (bottom) for $[\mathbf{1}(F)]^{7+}$.

## 4. Formation of tetrahedral host-guest complexes $(C_{60})_{1\text{-}3}\subset$**1** using $MeNO_2$

A J-Young NMR tube was charged with **1**$(BF_4)_8$ (6.0 mg, 1.0 umol) dissolved in $CD_3NO_2$ (0.5 mL). $C_{60}$ (7.2 mg, 10 μmol, 10 equiv) was added and the vessel was placed under a $N_2$ atmosphere by undergoing three freeze/pump/thaw cycles. The mixture was sonicated for 30 min, then stirred at 298 K for 6 h. The suspension containing residual $C_{60}$ was centrifuged. The supernatant was collected and dried to yield $(C_{60})_{1\text{-}3}\subset$**1**.

Note: Prolonged stirring (>48 h) at 298 K led to the partial transformation of the tetrahedral host-guest complexes into $C_{60}\subset$**2**.

$^1$H NMR (400 MHz, 298 K, $CD_3NO_2$): $\delta$ 10.13 – 9.67 (m, 12H), 9.47 (s, 12H), 8.99 – 8.92 (m, 12H), 8.57 (br, 12H), 8.19 – 7.98 (m, 24H), 7.79 (br, 24H), 6.92 (br, 24H), 3.67 (br, 48H), 2.27 (s, 72H), 1.72 – 1.36 (m, br, 72H) ppm. See Figure S7 for assignments.

$^{13}$C NMR (125 MHz, 298 K, $CD_3NO_2$): $\delta$ 171.2, 154.8, 152.1, 147.8, 142.3, 136.8, 136.6, 136.4, 136.0, 135.9, 135.2, 135.0, 134.1, 130.4, 127.8, 127.0, 117.3, 111.4, 92.5, 27.6, 25.3, 25.3, 25.0, 15.2, 12.5, 11.5 ppm.

LR-ESI-MS [charge, calculated for $Fe_4(C_{56}H_{52}N_8Ni)_6(C_{60})_y(BF_4)_{(8-x)}(F)_x$]: *m/z* = 1298.8 [$(C_{60})_3\subset$**1**$(F)_2^{6+}$, 1299.6], 1179.1 [$(C_{60})_2\subset$**1**$(F)_2^{6+}$, 1179.5], 1110.9 [$(C_{60})_3\subset$**1**$(F)]^{7+}$, 1111.2], 1059.7 [$C_{60}\subset$**1**$(F)_2^{6+}$, 1059.4], 1008.5 [$(C_{60})_2\subset$**1**$(F)^{7+}$, 1008.3], 969.7 [$(C_{60})_3\subset$**1**$^{8+}$, 969.9], 904.6 [$C_{60}\subset$**1**$(F)^{7+}$, 905.3], 879.7 [$(C_{60})_2\subset$**1**$^{8+}$, 879.9], 802.2 [**1**$(F)^{7+}$, 802.4], 789.8 [$C_{60}\subset$**1**$^{8+}$, 789.8], 699.8 [**1**$^{8+}$, 699.7].

HR-ESI-MS calculated for $C_{60}\subset$**1**$^{8+}$ *m/z* = 789.7439, found 789.7435.
HR-ESI-MS calculated for $(C_{60})_2\subset$**1**$^{8+}$ *m/z* = 879.8692, found 879.8697.
HR-ESI-MS calculated for $(C_{60})_3\subset$**1**$^{8+}$ *m/z* = 969.8694, found 969.8685.

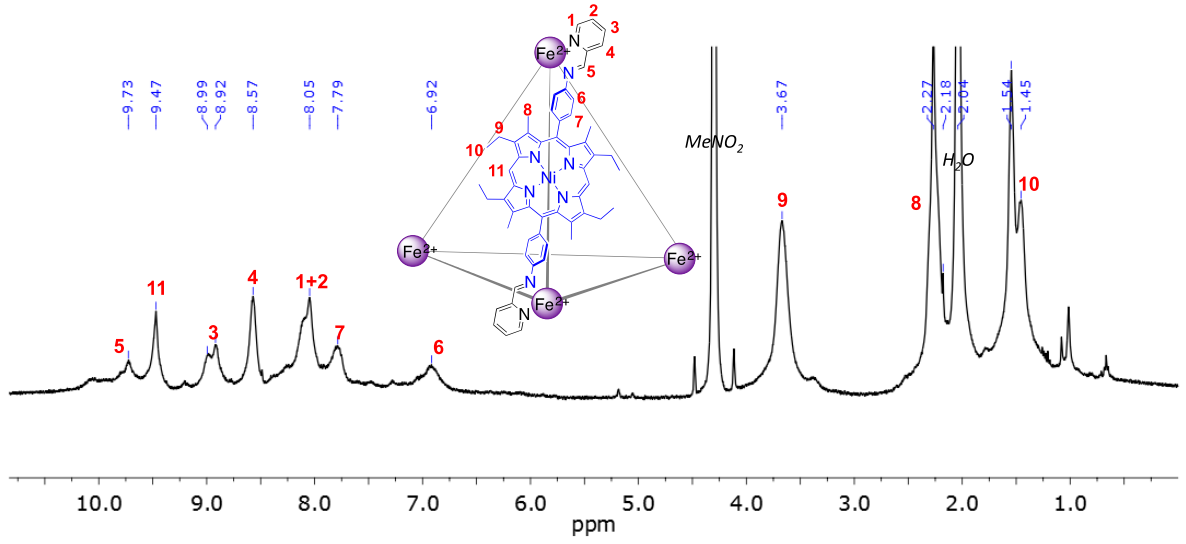


**Figure S7.** $^{1}$H NMR spectrum (400 MHz, 298 K, $CD_3NO_2$) of $(C_{60})_{1\text{-}3}\subset$**1**.

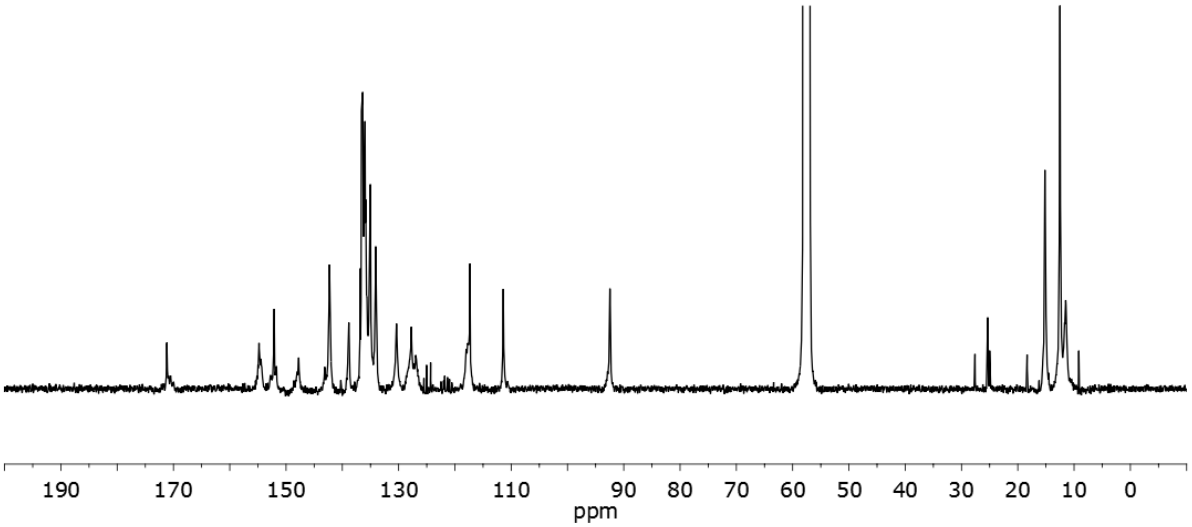


**Figure S8.** $^{13}$C NMR (125 MHz, 298 K, $CD_3NO_2$) spectrum of $(C_{60})_{1\text{-}3}\subset$**1**.

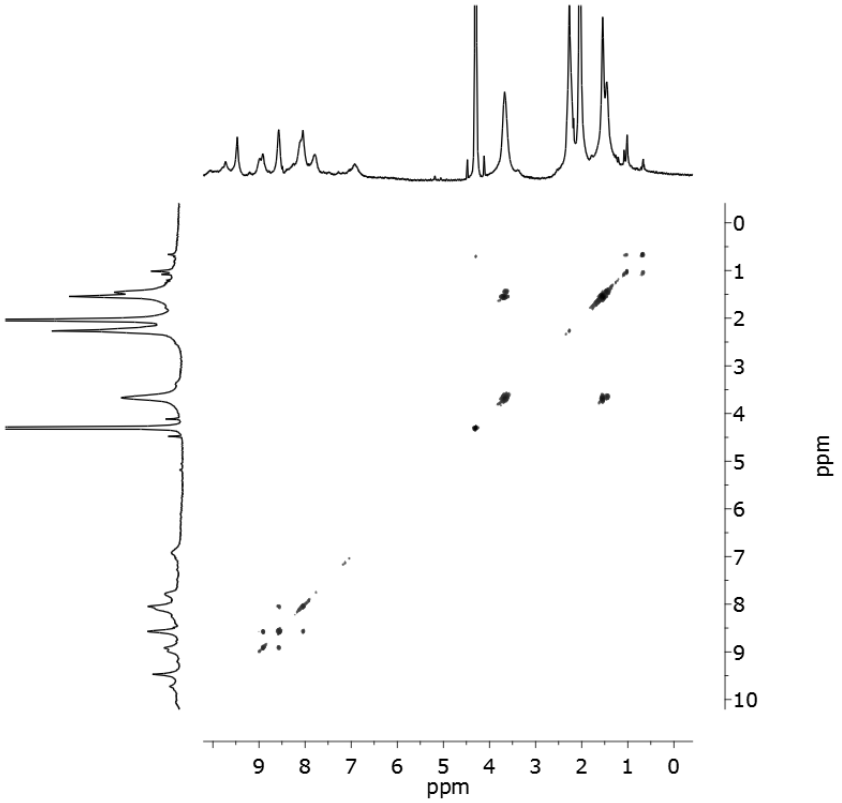


**Figure S9.** $^{1}$H-$^{1}$H COSY spectrum (400 MHz, 298 K, $CD_3NO_2$) of $(C_{60})_{1\text{-}3}\subset$**1**.

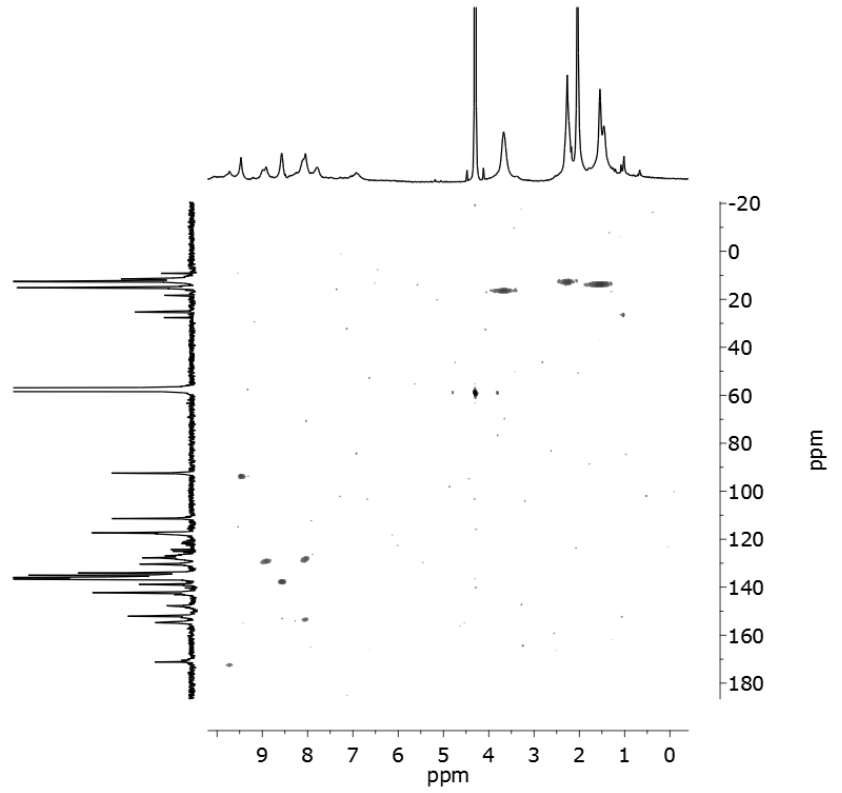


**Figure S10.** $^{1}$H-$^{13}$C HSQC spectrum (400 MHz, 298 K, $CD_3NO_2$) of $(C_{60})_{1\text{-}3}\subset$**1**.

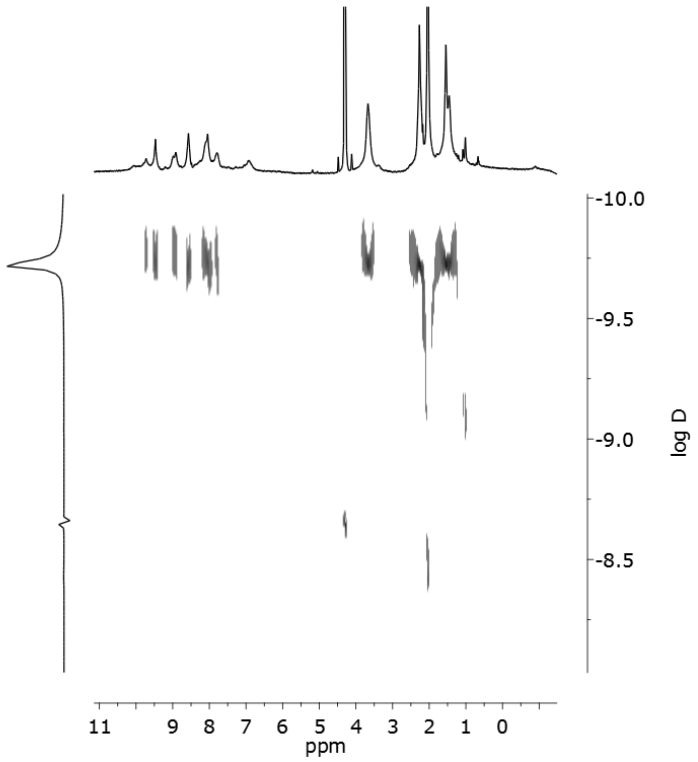


**Figure S11.** $^{1}$H-DOSY (400 MHz, 298 K, $CD_3NO_2$) spectrum of $(C_{60})_{1\text{-}3}\subset$**1**.

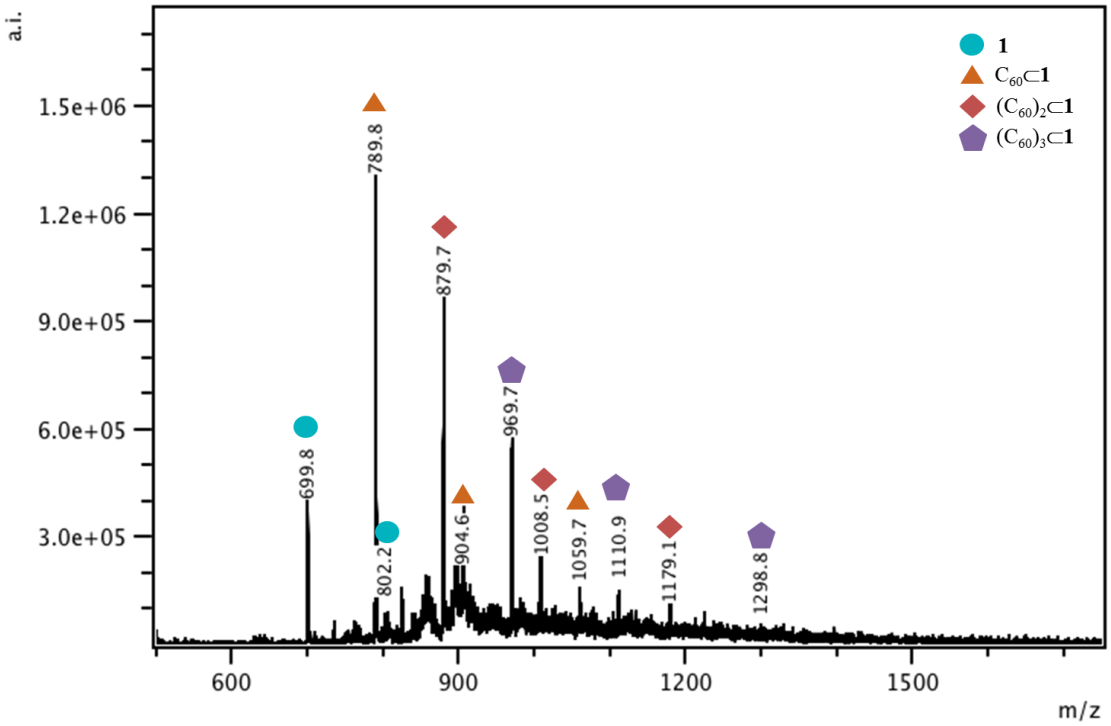


**Figure S12.** ESI mass spectrum of $(C_{60})_{1\text{-}3}\subset$**1**. Each labeled signal corresponds to the tetrahedral complex with a number of $F^-$ counterions. The fluoride observed by ESI-MS presents as an impurity in the metal salt used in the synthesis of **1**.

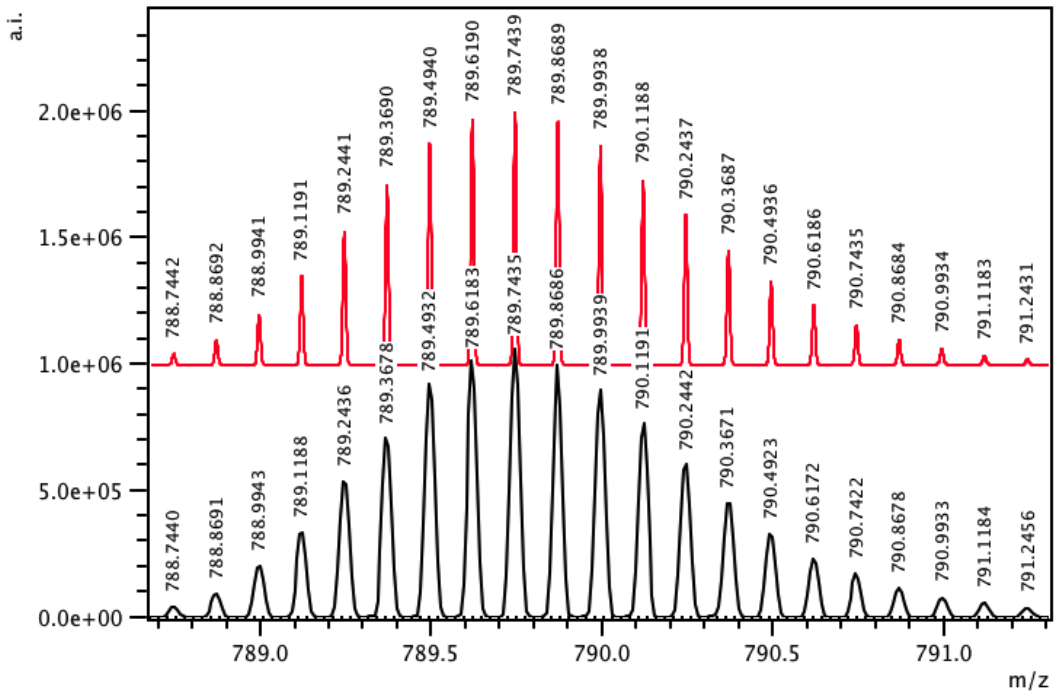


**Figure S13.** High resolution ESI mass spectrum analysis of $C_{60}\subset\mathbf{1}(BF_4)_8$, showing the theoretical isotope model (top) and the observed data (bottom) for $C_{60}\subset\mathbf{1}^{8+}$.

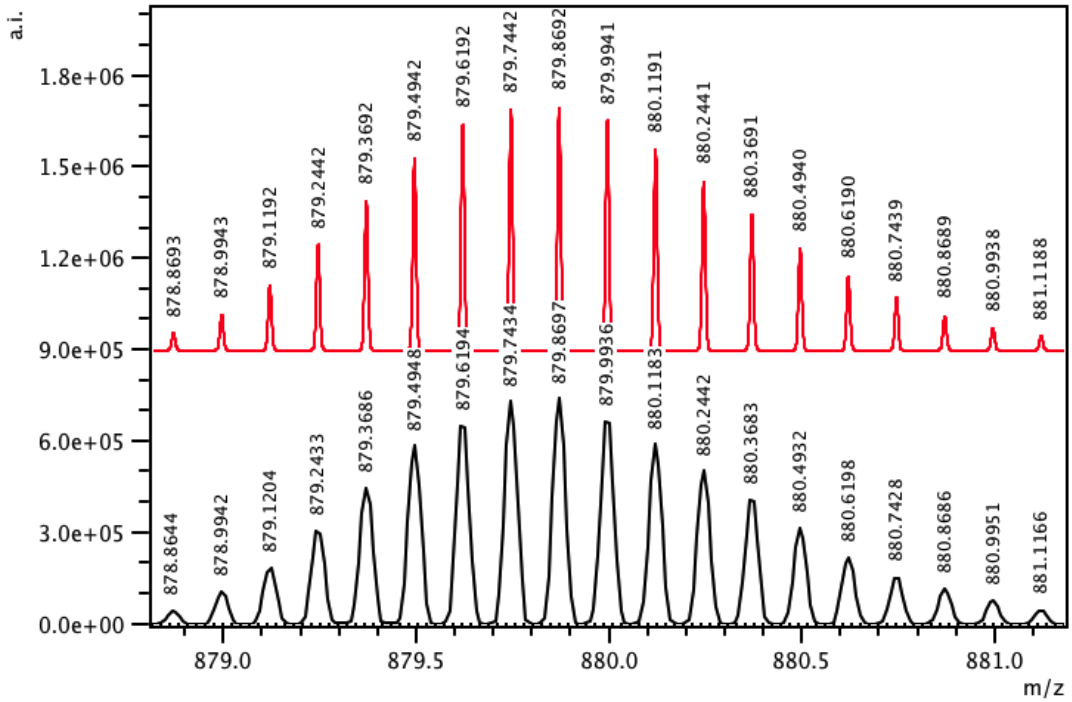


**Figure S14.** High resolution ESI mass spectrum analysis of $(C_{60})_2\subset\mathbf{1}(BF_4)_8$, showing the theoretical isotope model (top) and the observed data (bottom) for $(C_{60})_2\subset\mathbf{1}^{8+}$.

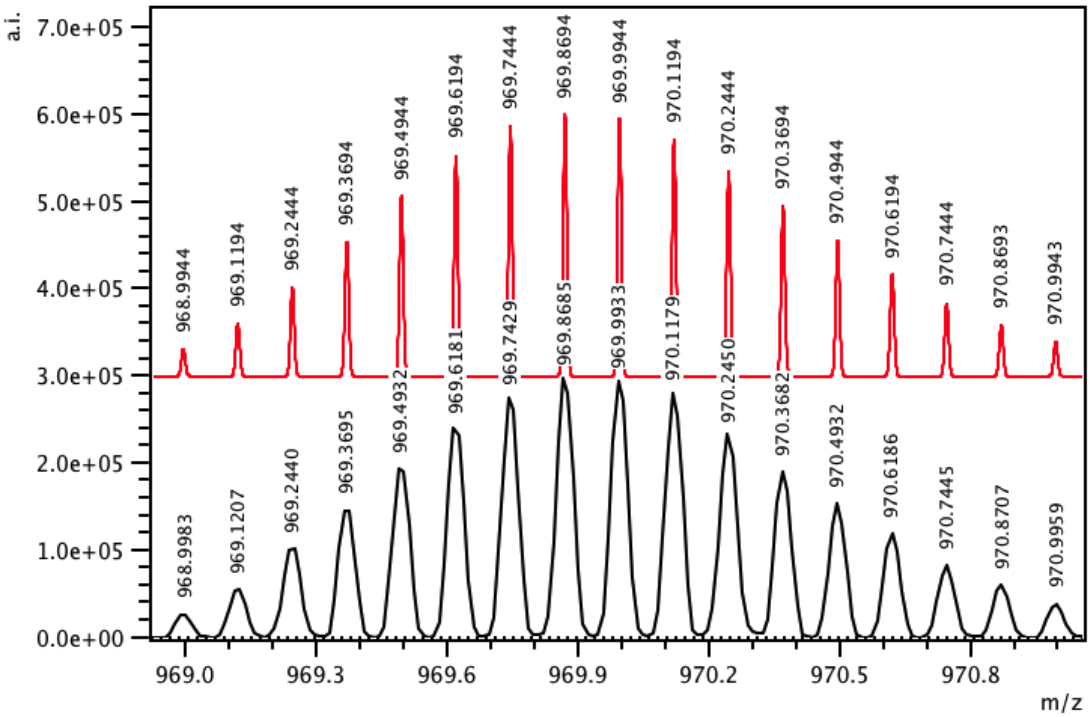


**Figure S15.** High resolution ESI mass spectrum analysis of $(C_{60})_3\subset\mathbf{1}(BF_4)_8$, showing the theoretical isotope model (top) and the observed data (bottom) for $(C_{60})_3\subset\mathbf{1}^{8+}$.

## 5. Formation of $Fe^{II}_3L_4$ host-guest complex $C_{60}\subset$**2** using MeCN

A J-Young NMR tube was charged with **Ni-NH2** (6.0 mg, 8.4 μmol, 6 equiv) $Fe(BF_4)_2{\cdot}6H_2O$ (2.5 mg, 7.4 μmol, 5.3 equiv), 2-formylpyridine (1.7 μL, 16.8 μmol, 12 equiv) and $CD_3CN$ (0.5 mL). The vessel was placed under a $N_2$ atmosphere by undergoing three freeze/pump/thaw cycles. The mixture was then sonicated for 30 min and stirred at 343 K for 6 h to yield **1**. $C_{60}$ (10.1 mg, 14.0 μmol, 10 equiv) was added and the mixture was sonicated for a further 30 min, then stirred at 298 K for 22 h. The mixture was filtered and the solvent evaporated to yield $C_{60}\subset$**2**. Some evidence of tetrahedral host-guest complexes $(C_{60})_{1\text{-}3}\subset$**1** was observed by ESI-MS.

$^1$H NMR (500 MHz, 298 K, $CD_3CN$): $\delta$ 9.88 (s, 2H), 9.64 (s, 2H), 9.52 (s, 2H), 9.45 (s, 4H), 9.06 (s, 2H), 8.98 (d, $J$ = 7.2 Hz, 2H), 8.94 – 8.83 (m, 4H), 8.82 – 8.73 (m, 4H), 8.67 – 8.37 (m, 12H), 8.08 – 7.78 (m, 16H), 7.49 – 7.37 (m, 2H), 7.30 (s, 2H), 6.71 – 6.48 (m, 6H), 6.43 (d, $J$ = 6.9 Hz, 2H), 6.35 (d, $J$ = 7.4 Hz, 2H), 5.90 (d, $J$ = 7.0 Hz, 2H), 5.84 (d, $J$ = 6.5 Hz, 2H), 5.06 (d, $J$ = 7.9 Hz, 2H), 3.99 – 3.31 (m, 32H), 2.71 (s, 8H), 2.29 – 2.01 (m, 40H), 1.85 – 1.09 (m, 48H) ppm. See Figure S16 for full assignment.

$^{13}$C NMR (125 MHz, 298 K, $CD_3CN$): $\delta$ 205.2, 203.9, 203.6, 203.3, 188.1, 187.7, 187.1, 186.7, 185.5, 184.0, 181.4, 180.6, 180.3, 179.2, 176.5, 176.2, 175.8, 175.6, 174.9, 174.3, 170.8, 170.2, 169.6, 169.1, 168.9, 168.1, 167.7, 166.9, 165.9, 165.3, 163.9, 163.7, 161.7, 160.7, 160.5, 160.0, 159.7, 126.8, 126.2, 125.8, 60.9, 58.6, 58.5, 58.3, 56.1, 51.7, 48.4, 48.1, 47.9, 46.9, 46.6, 46.2, 45.9, 45.6, 45.1, 44.9, 44.5, 44.3, 44.0, 43.6, 43.1, 42.7 ppm.

LR-ESI-MS [charge, calculated for $Fe_3(C_{56}H_{52}N_8Ni)_4(C_{60})(BF_4)_{(6\text{-}x)}(F)_x$]: *m/z* = 1576.7 [$C_{60}\subset$**2**$(BF_4)_3^{3+}$, 1577.2], 1554.1 [$C_{60}\subset$**2**$(F)(BF_4)_2^{3+}$, 1554.6], 1531.8 [$C_{60}\subset$**2**$(F)_2(BF_4)^{3+}$, 1532.0], 1144.7 [$C_{60}\subset$**2**$(F)(BF_4)^{4+}$, 1144.3], 1127.5 [$C_{60}\subset$**2**$(F)_2^{4+}$, 1127.3], 898.3 [$C_{60}\subset$**2**$(F)^{5+}$, 898.0], 758.9 [$C_{60}\subset$**2**$(MeCN)_2^{6+}$, 758.9], 751.8 [$C_{60}\subset$**2**$(MeCN)^{6+}$, 752.0].

HR-ESI-MS calculated for $C_{60}\subset$**2**$(MeCN)^{6+}$ *m/z* = 752.0512, found 752.0481.

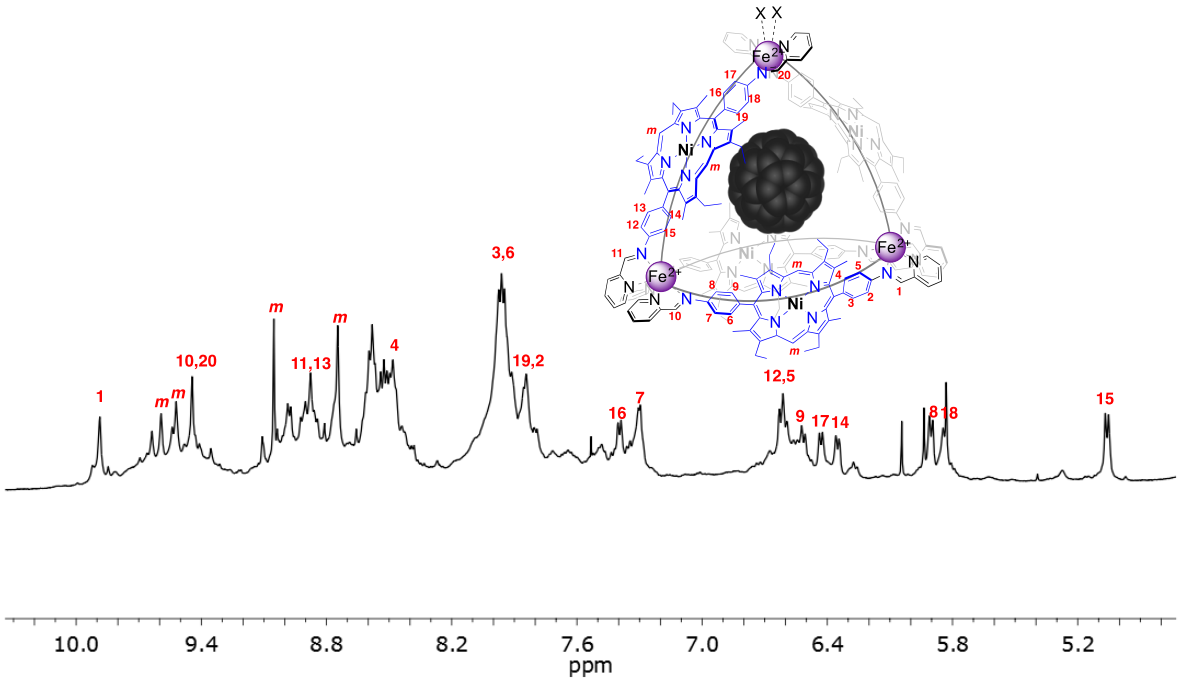


**Figure S16.** The aromatic region of the $^{1}$H NMR spectrum of $C_{60}\subset$**2** (500 MHz, 298 K, $CD_3CN$) with resonance assignment. The pyridyl proton resonances overlapped to such an extent that unambiguous assignment was not possible.

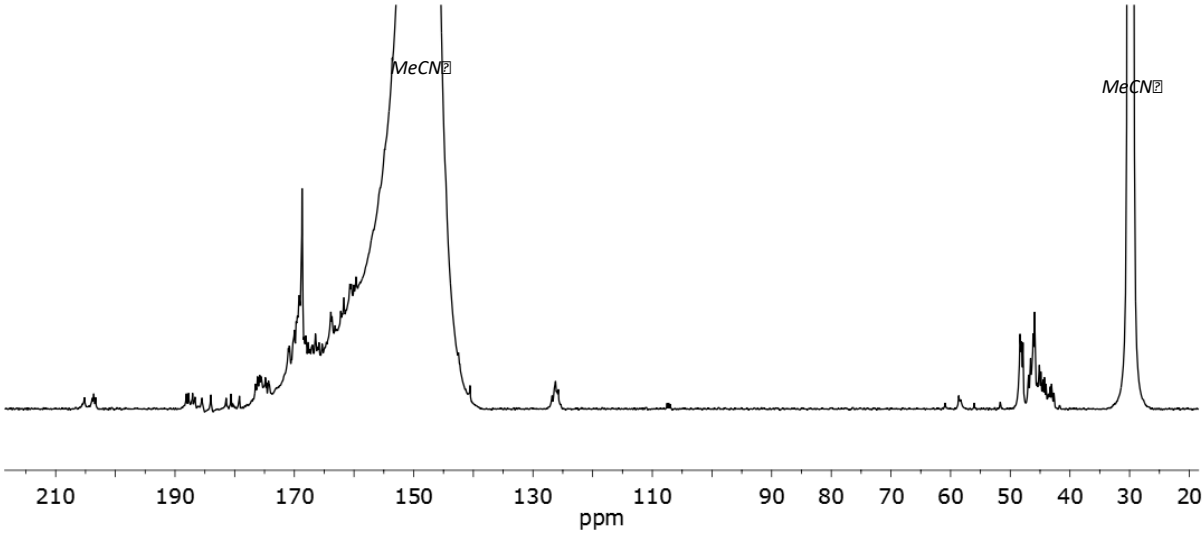


**Figure S17.** $^{13}$C NMR spectrum (125 MHz, 298 K, $CD_3CN$) of $C_{60}\subset$**2**.

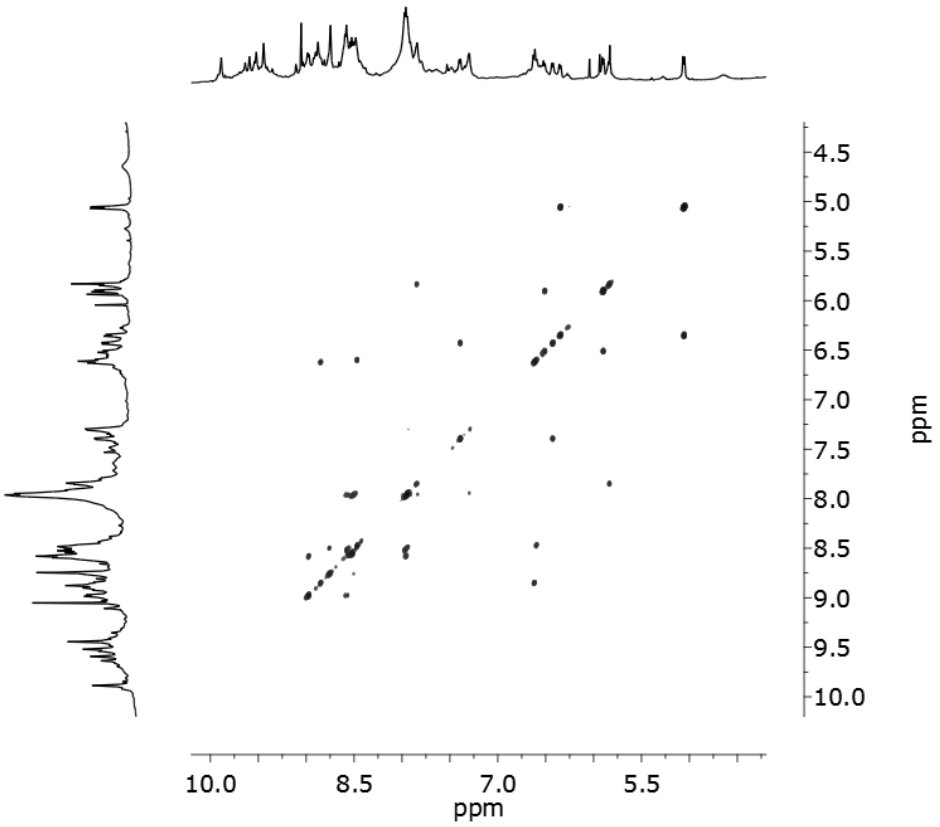


**Figure S18.** $^{1}$H-$^{1}$H COSY spectrum (500 MHz, 298 K, $CD_3CN$) of the aromatic region of $C_{60}$⊂**2**.

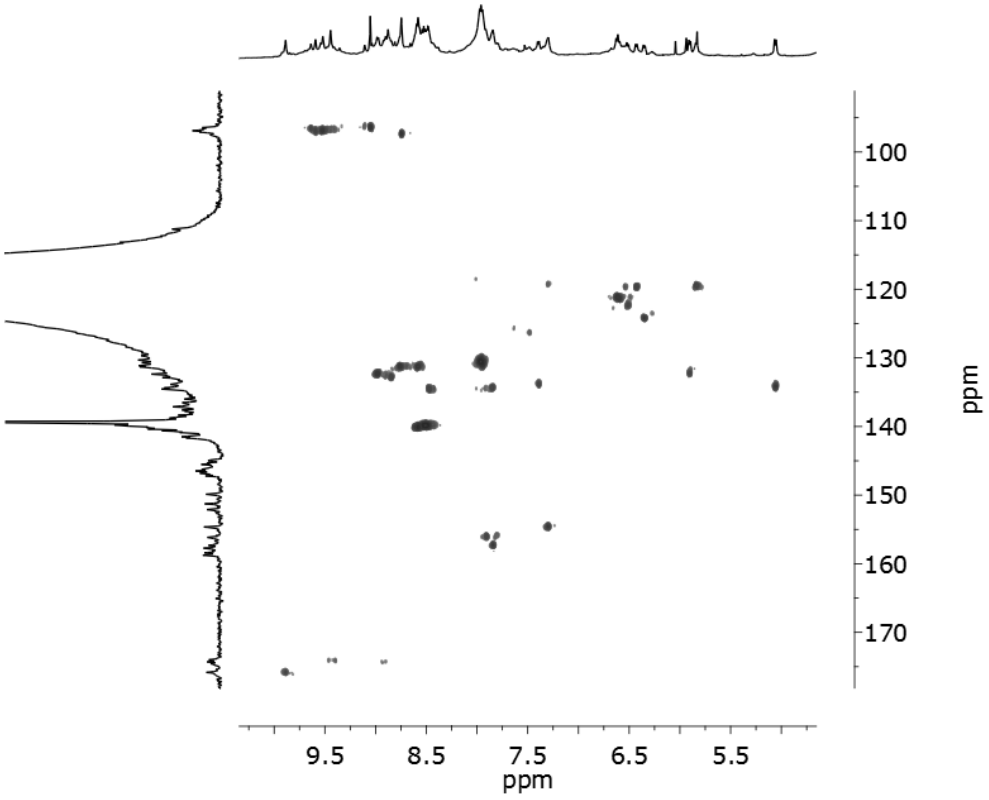


**Figure S19.** $^{1}$H-$^{13}$C HSQC spectrum (500 MHz, 298 K, $CD_3CN$) of the aromatic region of $C_{60}$⊂**2**.

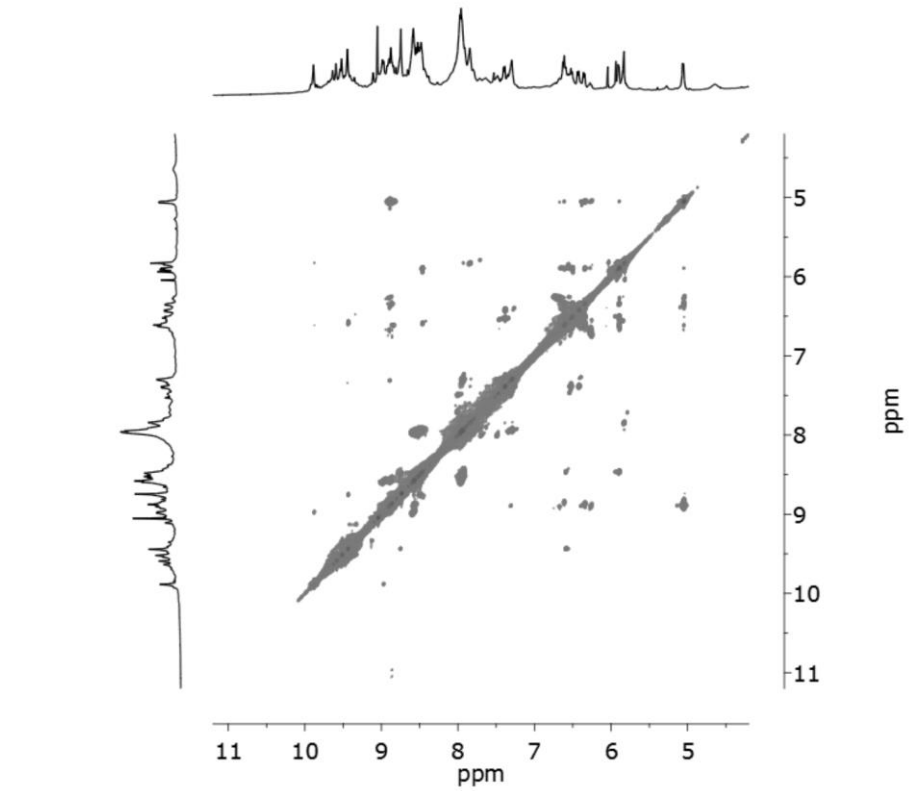


**Figure S20.** $^{1}$H-$^{1}$H NOESY spectrum 500 MHz, 298 K, $CD_3CN$) of the aromatic region of $C_{60}\subset$**2**.

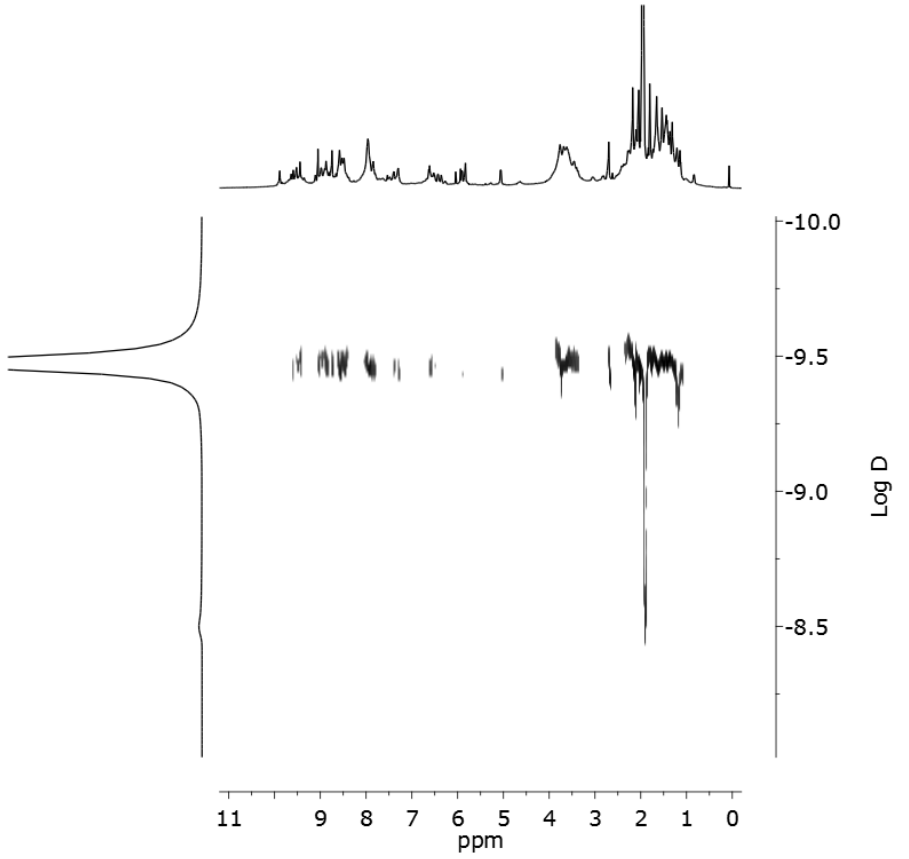


**Figure S21.** $^{1}$H-DOSY spectrum (400 MHz, 298 K, $CD_3CN$) of $C_{60}\subset$**2**.

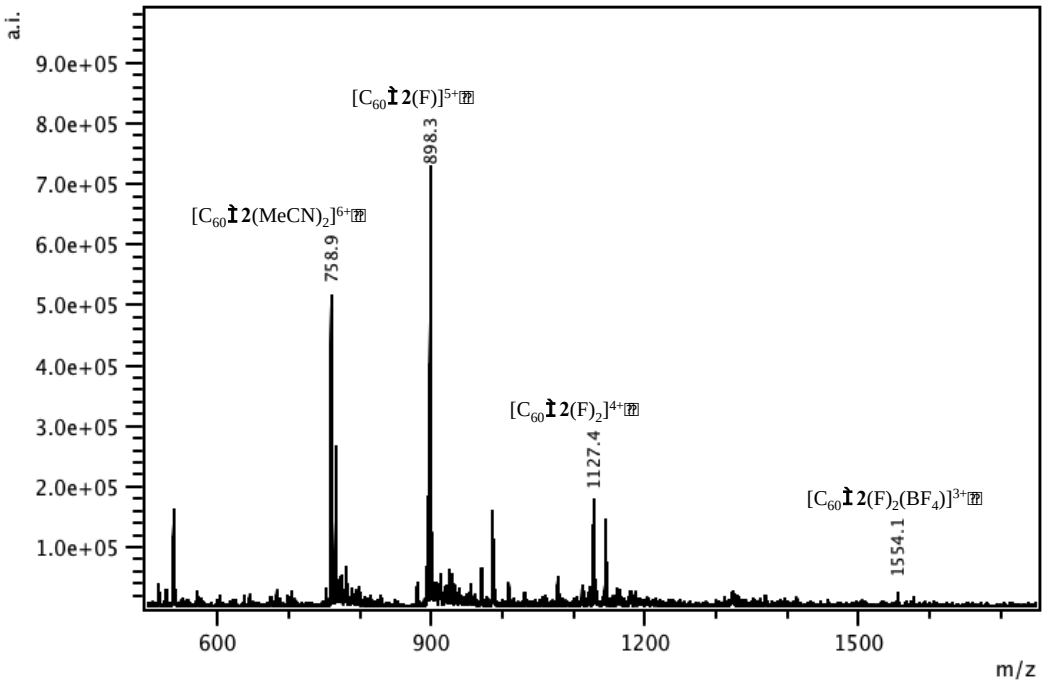


**Figure S22.** Low resolution ESI mass spectrum of $C_{60}\subset$**2** with the major signals labelled. A full signal list is included in the experimental. Again, $F^-$ was observed as an impurity in the metal salt employed during synthesis.

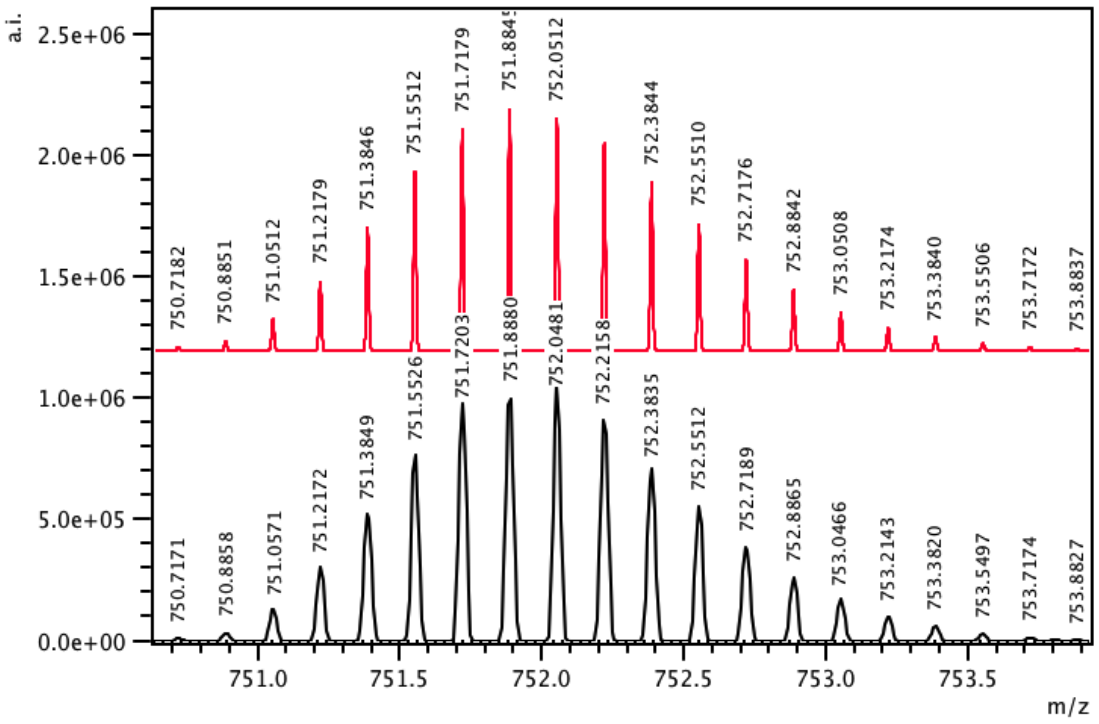


**Figure S23.** High resolution ESI mass spectrum of $C_{60}\subset$**2**$(BF_4)_6$, showing the theoretical isotope model (top) and the observed data (bottom) of $C_{60}\subset$**2**$(MeCN)^{6+}$.

## 6. Formation of $(C_{60})_{1\text{-}4}\subset$**1** using $PhNO_2$

A sample of **1**$(BF_4)_8$ (6.0 mg, 0.96 μM) was dissolved in nitrobenzene (1 mL). $C_{60}$ (15 mg, 20.9 μM) was added. The mixture was sonicated for five minutes then stirred at room temperature for 24 h. The sample was added dropwise to $Et_2O$ and filtered through Celite. The solid residue was dissolved in $MeNO_2$ or MeCN, centrifuged to remove unbound $C_{60}$ and the supernatant decanted. The solution was dried to yield $(C_{60})_{1\text{-}4}\subset$**1**.

Samples of $(C_{60})_{1\text{-}4}\subset$**1** formed in $PhNO_2$ showed no sign of redistribution to the 1-3 adduct by ESI-MS after 8 hours standing at RT in $CH_3CN$. This suggests stability of the respective host-guest occupancies over the course of the electrochemical and spectroscopic experiments (see below).

$^1$H NMR (500 MHz, 298 K, $d_5$-$PhNO_2$): 9.29 (12H), 8.65 (24H), 8.14 (12H), 7.73 (12H), 7.57 (12H), 7.06 (24H), 5.58 (24H), 3.3 – 2.8 (br, 48H), 2.0 – 1.7 (br, 72H), 1.0 – 0.6 (br, 72H) ppm.

$^{13}$C NMR (125 MHz, 298 K, $d_5$-$PhNO_2$): $\delta$ 175.3, 155.5, 141.3 (broad, $C_{60}$), 140.1, 130.8, 130.1, 95.4, 19.6–18.0, 17.8–15.3, 16.8–13.7 ppm. Reported $^{13}$C signals for the cage are only those that could be identified from the $^1$H-$^{13}$C HSQC spectrum.

LR-ESI-MS [charge, calculated for $Fe_4(C_{56}H_{52}N_8Ni)_6(C_{60})_x(BF_4)_8$]: *m/z* = 1604.1 $[(C_{60})_3\subset$**1**$(BF_4)_3]^{5+}$, 1604.1], 1442.5 $[(C_{60})_4\subset$**1**$(BF_4)_2]^{6+}$, 1442.4], 1322.1 $[(C_{60})_3\subset$**1**$(BF_4)_2]^{6+}$, 1322.3], 1223.3 $[(C_{60})_4\subset$**1**$(BF_4)]^{7+}$, 1223.9], 1121.0 $[(C_{60})_3\subset$**1**$(BF_4)]^{7+}$, 1121.0], 1060.0 $[(C_{60})_4\subset$**1**$]^{8+}$, 1060.1], 970.0 $[(C_{60})_3\subset$**1**$]^{8+}$, 970.0] 880.0 $[(C_{60})_2\subset$**1**$]^{8+}$, 880.0], 789.7 $[C_{60}\subset$**1**$]^{8+}$, 789.8].

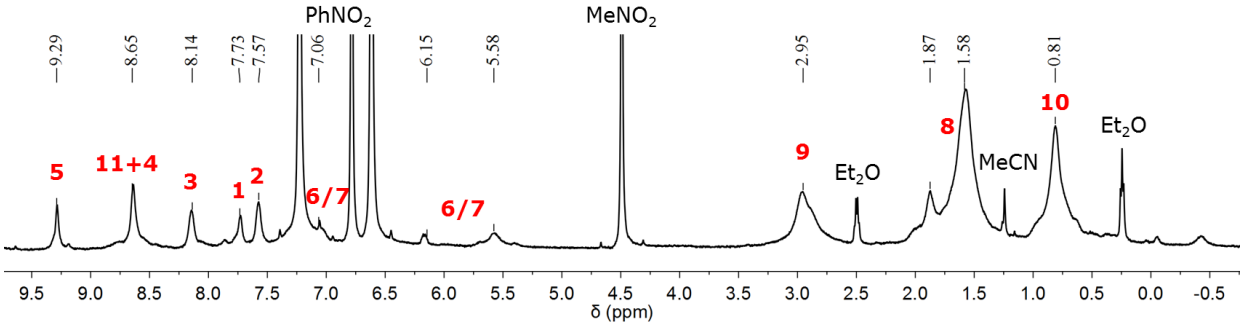


**Figure S24.** $^1$HNMR spectrum (500 MHz, 298 K, $d_5$-$PhNO_2$) of $(C_{60})_{1\text{-}4}\subset$**1**. The broad peaks of protons 6 and 7 prevented their definitive assignment. Number assignments correlate with the structure displayed in Figure S1.

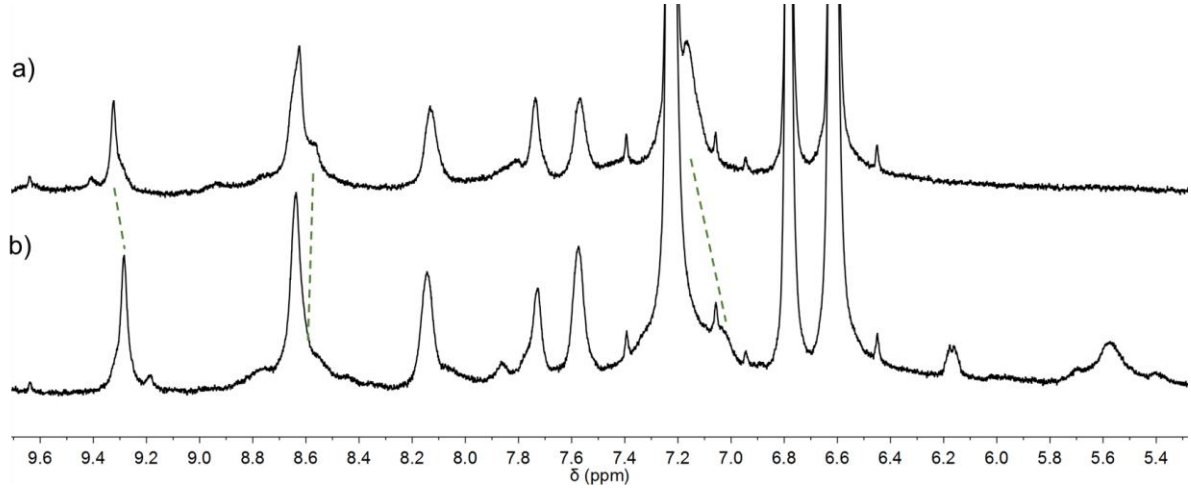


**Figure S25.** Aromatic region of the $^{1}$HNMR spectrum (500 MHz, 298 K, $d_5$-$PhNO_2$) of a) **1** and b) $(C_{60})_{1\text{-}4}\subset$**1** in $PhNO_2$. The most significant shifts were observed for the imine, phenylene and porphyrin protons upon fullerene binding.

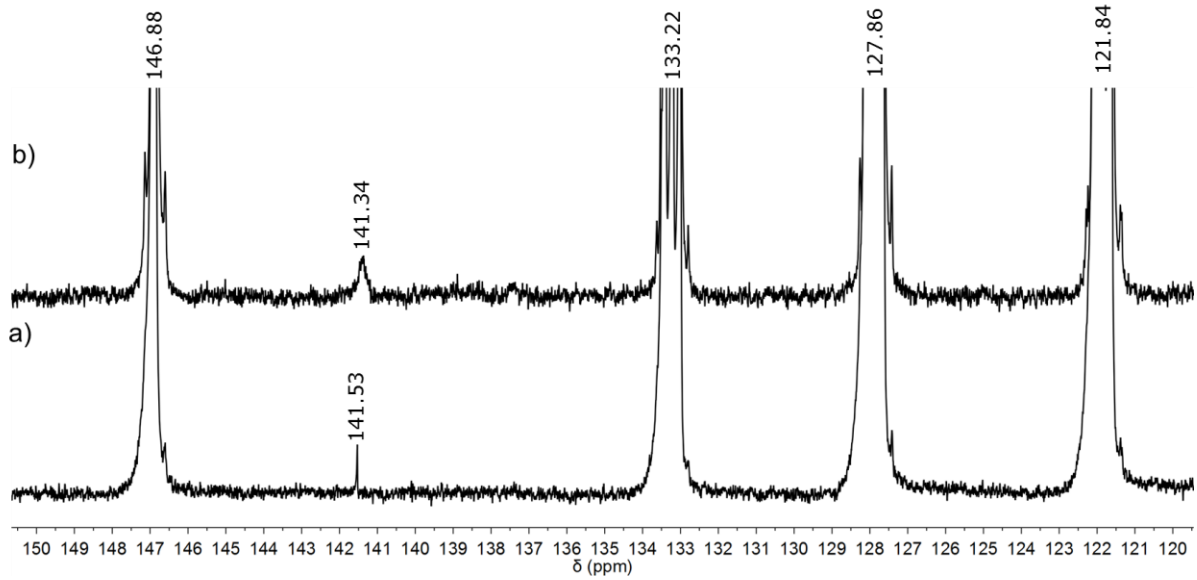


**Figure S26.** $^{13}$C NMR spectra (125 MHz, 298 K, $d_5$-$PhNO_2$) of a) free $C_{60}$ and b) $(C_{60})_{1\text{-}4}\subset$**1** in $PhNO_2$. Broadening and shifting of the $^{13}$C signal of $C_{60}$ indicates fast-exchange binding within the cavity of **1** in $PhNO_2$.

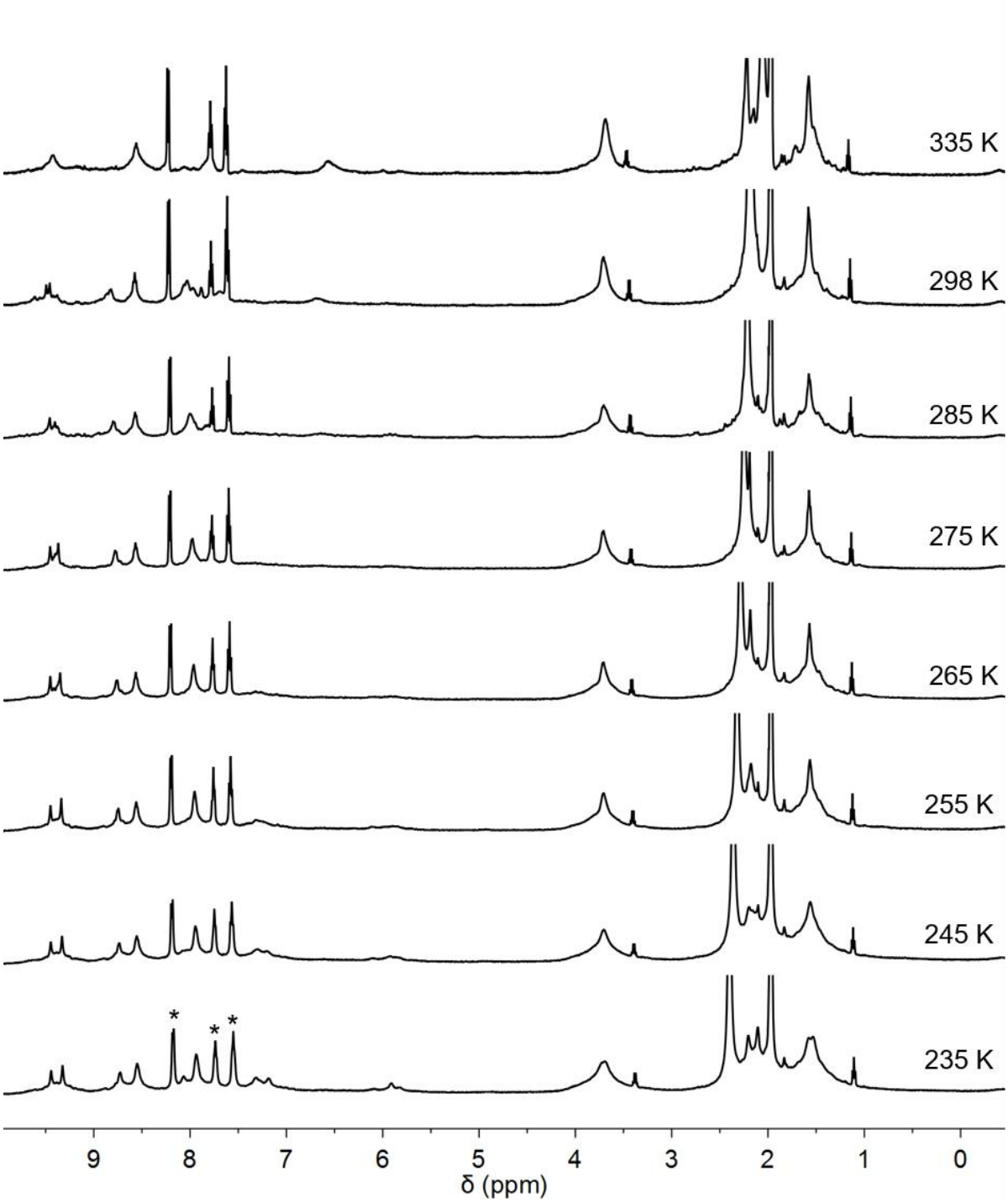


**Figure S27.** Variable temperature $^{1}$H NMR spectra (500 MHz, $CD_3CN$) of $(C_{60})_{1\text{-}4}\subset$**1**. Residual $PhNO_2$ signals are marked *.

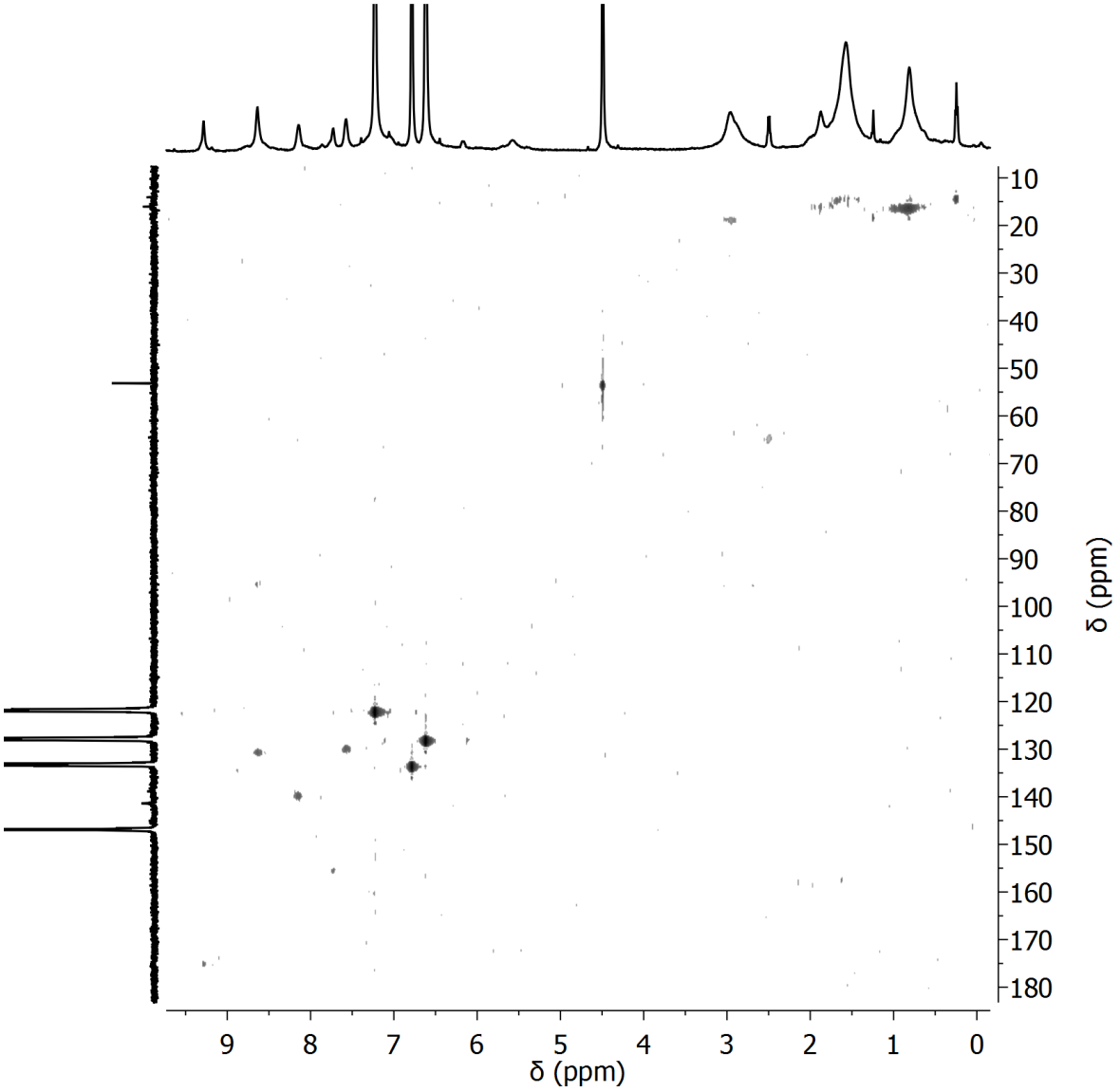


**Figure S28.** $^{1}H$-$^{13}C$ HSQC spectrum (500 MHz, 298 K, $d_5$-$PhNO_2$) of $(C_{60})_{1\text{-}4}\subset$**1** in $PhNO_2$.

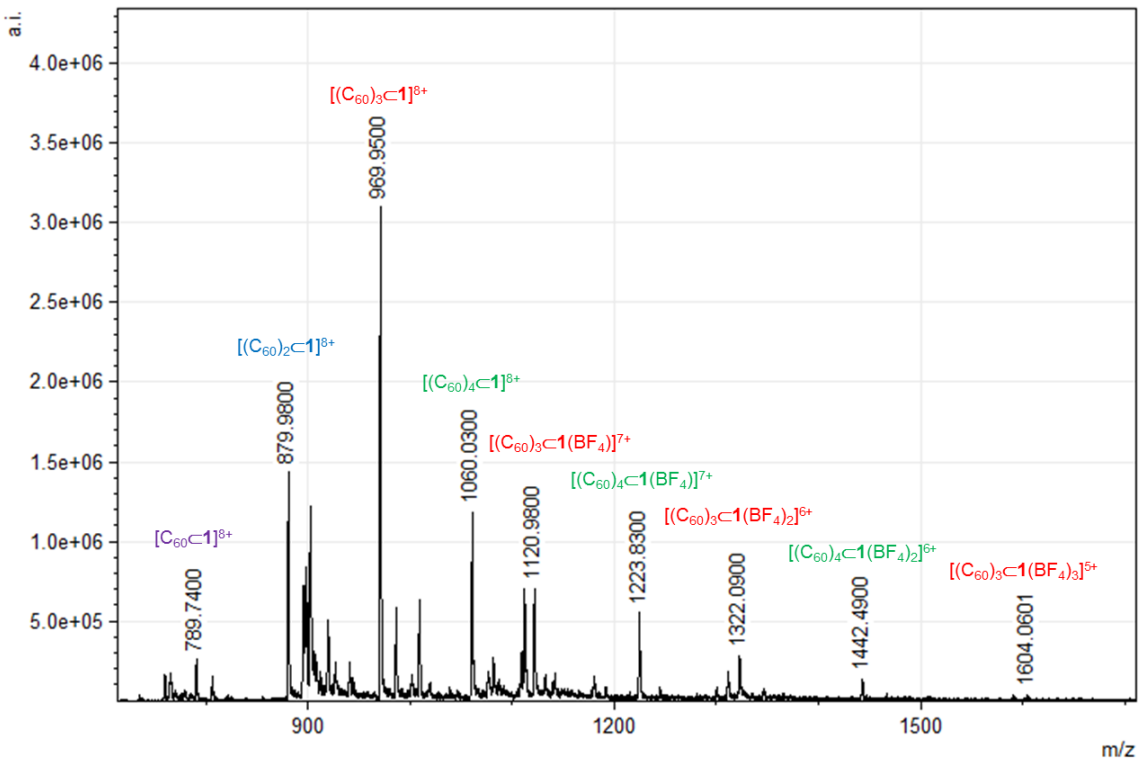


**Figure S29.** Low resolution ESI mass spectrum of $(C_{60})_{1\text{-}4}\subset\mathbf{1}$. Each colour corresponds to a different number of fullerenes within **1** when synthesised in $PhNO_2$ (green = $(C_{60})_4\subset\mathbf{1}$, red = $(C_{60})_3\subset\mathbf{1}$, blue = $(C_{60})_2\subset\mathbf{1}$, purple = $C_{60}\subset\mathbf{1}$).

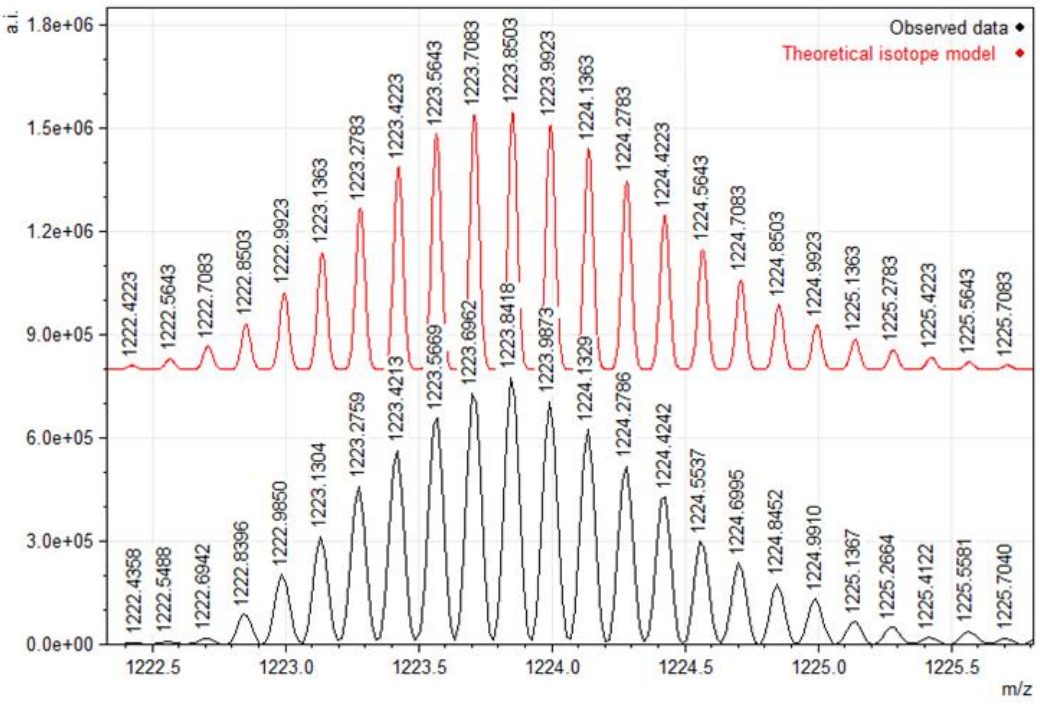


**Figure S30.** HRMS analysis of $(C_{60})_4\subset\mathbf{1}(BF_4)_8$ showing the theoretical isotope model (top) and the observed data (bottom) for $(C_{60})_4\subset\mathbf{1}(BF_4)^{7+}$.

## 7. The binding of multiple fullerenes within **1**

### 7.1 Addressing the mode of fullerene binding

Host **1** is a multivalent receptor; fullerenes can bind to up to four binding sites. Firstly, we addressed the simplest case, wherein the interaction between fullerenes was assumed to be non-cooperative. To achieve this, we examined the binding of a fullerene, G, with one of the binding sites, H.

H + G ⇌ HG

In this way, we can determine the intrinsic binding constant, $K_{int}$, by assuming a 1:1 interaction between fullerenes and each individual binding site of **1**.

$$K_{int} = \frac{[HG]}{[G][H]}$$

The data can then be fitted to a 1:1 binding model, where the total concentration of binding pockets is four times the total concentration of host, since host **1** has four binding pockets. This is equivalent to a non-cooperative 1:4 binding model for the host.

Knowing that $K_{int}$ is the ratio between the binding constant for each step *i* ($K_i$) and a statistical factor $\Omega_i$ (Equation S3.3), it is then possible to calculate the binding constant between host **1** and $C_{60}$ for each successive binding step.

$K_i = \Omega_i K_{int}$

By applying this method, we observed sigmoidal residuals and high fitting covariances for the non-cooperative model, where the concentration of binding sites was $2.26 \times 10^5$ M (Figure S32).

When a cooperative 1:2 model was employed (where the concentration is that of the cage, $5.65\times 10^6$ M), random residuals and a lower covariance (an order of magnitude lower than for the non-cooperative model) were observed (Figure S33). Equations for the 1:1 and 1:2 models are available in the review by Thordarson.[3] We hypothesize that the third and fourth binding events are either not observed at low concentrations ($5.65 \times 10^{-6}$ M), or are significantly weak to prevent their observation by absorption spectroscopy.

With four potential binding sites, statistical factors must be applied to account for the binding microstates. Here, $K_1 = 4k$, $K_2 = 3/2k$, $K_3 = 2/3k$ and $K_4 = 1/4k$. The ratio of $K_2/K_1$ is thus described as

$$\frac{K_2}{K_1} = \frac{\frac{3}{2}k}{4k} = \frac{3}{8}$$

And the cooperativity parameter $\alpha$ is described as

$$a = \frac{8K_2}{3K_1}$$

Where α > 1 is positive cooperativity and α < 1 is negative cooperativity for the first two binding events.

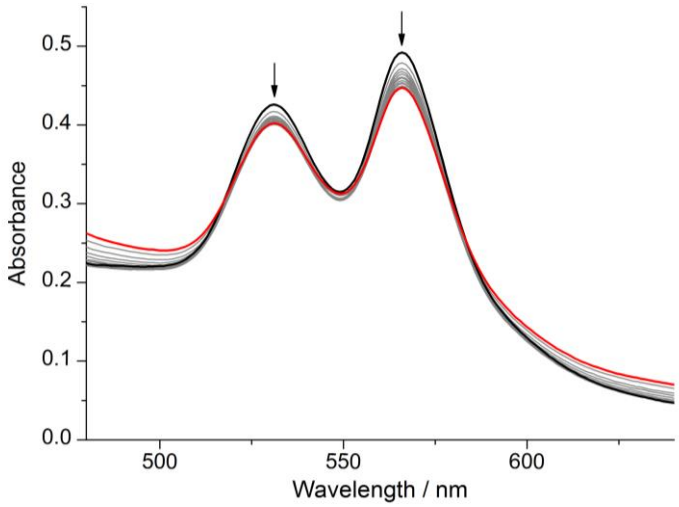


**Figure S31.** UV-Vis titration of $C_{60}$ into **1** in $PhNO_2$. The absorbance of $C_{60}$ have been subtracted in each spectrum. The black trace is the spectrum of the initial solution (0 eq. $C_{60}$) and the red trace is the final spectrum (35 eq. $C_{60}$).

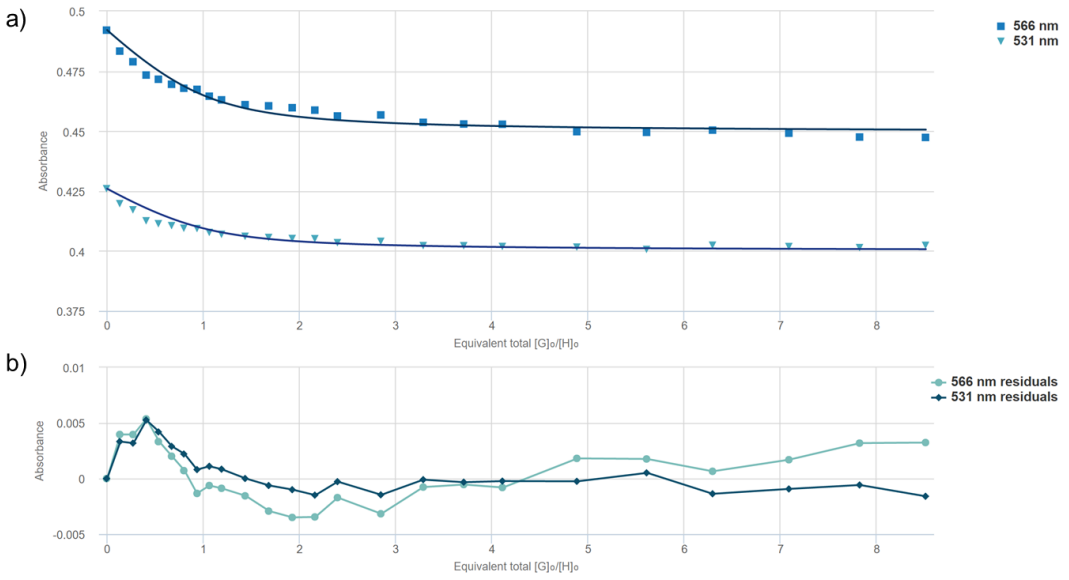


c)

Parameters

| Parameter (bounds) | Optimised | Error |
|---|---|---|
| K ( 0 → ∞ ) | 214706.98 M⁻¹ | ± 21.0540 % |

Quality of fit

| Fit | RMS | Covariance |
|---|---|---|
| 566 nm | 2.5214e-3 | 4.6314e-2 |
| 531 nm | 1.9439e-3 | 0.0887 |
| Total | 2.2513e-3 | 4.0065e-2 |

**Figure S32.** a) Titration data fitted to a non-cooperative model, wherein the concentration of binding sites is used, rather than the concentration of host; b) the residuals from the fit; and c) the parameters extracted from the fitting process. The presence of sigmoidal residuals, high fitting errors and high covariances indicates that a non-cooperative model is not appropriate to describe the binding of $C_{60}$ to **1**.

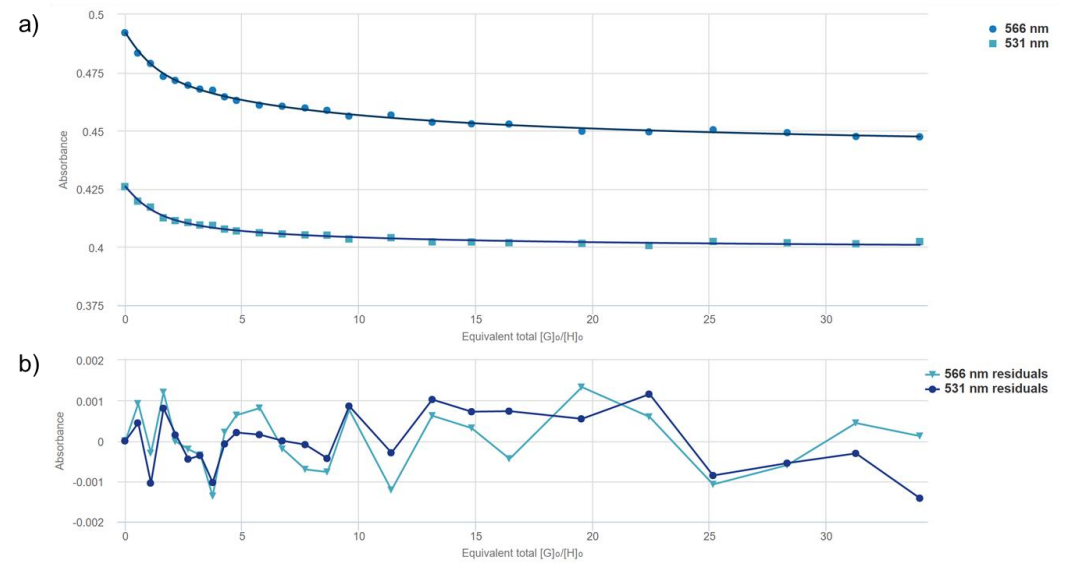


c)

Parameters

| Parameter (bounds) | Optimised | Error |
|---|---|---|
| $K_{11}$ ( 0 → ∞ ) | 301786.32 M⁻¹ | ± 11.6341 % |
| $K_{12}$ ( 0 → ∞ ) | 15560.66 M⁻¹ | ± 6.7382 % |

Quality of fit

| Fit | RMS | Covariance |
|---|---|---|
| 566 nm | 7.2846e-4 | 3.9700e-3 |
| 531 nm | 6.7325e-4 | 1.1632e-2 |
| Total | 7.0140e-4 | 4.0844e-3 |

**Figure S33.** a) Titration data fitted to a 1:2 cooperative model, wherein the concentration of the host is used; b) the residuals from the fit; and c) the parameters extracted from the fitting process. Low errors and a covariance an order of magnitude lower than that observed for the non-cooperative model indicates that a cooperative 1:2 model is more appropriate at describing the binding of $C_{60}$ to **1**.

### 7.2 Attempts to quantify the number of fullerenes in each assembly

It is not uncommon for a single species to crystallize selectively from a mixture, even if that product is not the major component of that mixture.[16] Different solvents likewise stabilize different crystal packing environments, promoting the crystallization of one product over another.[17] Structural differences were also observed between the two crystallized cage frameworks, indicating that different numbers of fullerenes (and their proximity to specific ligands) impacted upon the geometry of the cage. The ability for each of the unique host-guest products to pack in a crystal lattice is therefore different, affected by their distinct geometric differences. The crystallization of each of these system components from different solvent systems is therefore not necessarily representative of an increased concentration of the crystallized component in solution. A delicate balance of anion, solvents, structural rigidity and concentration are all necessary to obtain single crystals for X-ray studies. The selective crystallization of one of these components does not exclusively indicate its higher concentration in solution.

Despite employing numerous solvents (including chlorobenzene and benzonitrile) and purification methods (precipitation, trituration, size-exclusion column chromatography), pure samples of the individual host-guest complexes could not be obtained. Several techniques were employed to quantitatively gauge the distribution of host-guest complexes in $(C_{60})_{1\text{-}3}\subset$**1** and $(C_{60})_{1\text{-}4}\subset$**1**: the UV-vis spectra of $(C_{60})_{1\text{-}3}\subset$**1** and $(C_{60})_{1\text{-}4}\subset$**1** were indistinguishable, and their $^{1}$H NMR spectra displayed similar features (Figure S7 and S24). We hypothesised that comparison of the $^{13}$C spectra between these two assemblies would allow us to quantify the degree of fullerene encapsulation in each assembly by integrating the cage peaks against those of encapsulated $C_{60}$; however, as redistribution of the products was observed during our acquisition timescales, accurately measuring a $^{13}$C spectrum of suitable intensity proved challenging. Our only means of identifying the relative abundance of $C_{60}$ in these assemblies thus came from ESI-MS: these measurements showed that $(C_{60})_{1}\subset$**1** and $(C_{60})_{2}\subset$**1** were the dominant products in $(C_{60})_{1\text{-}3}\subset$**1**, whereas $(C_{60})_{3}\subset$**1** and $(C_{60})_{4}\subset$**1** are the dominant products in $(C_{60})_{1\text{-}4}\subset$**1** (Figure S12 and S29). This is consistent with $(C_{60})_{1\text{-}4}\subset$**1** having more fullerene present than in $(C_{60})_{1\text{-}3}\subset$**1**, supporting our conclusion that more fullerenes in the assembly reduce the reduction potential of the $C_{60}$ clusters.

## 8. Electrochemistry

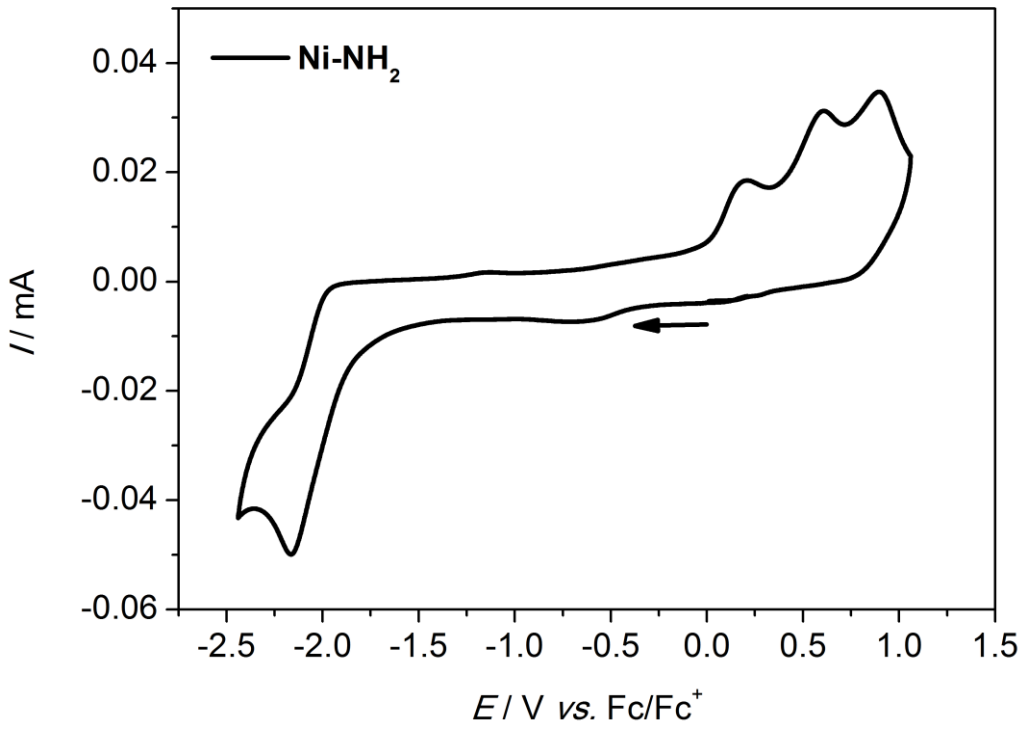


**Figure S34.** CV of ligand **Ni-NH$_2$** in 0.1 M *n*Bu$_4$NPF$_6$/CH$_2$Cl$_2$ electrolyte at 200 mV s$^{-1}$. The arrow indicates the direction of the forward scan.

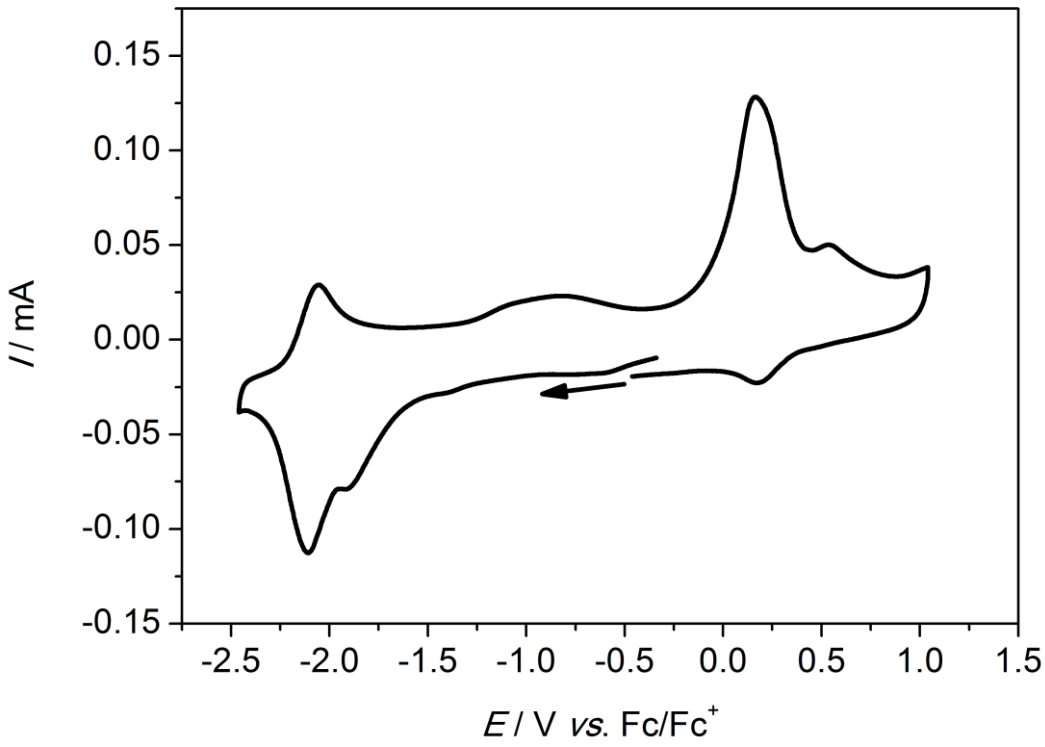


**Figure S35.** CV of cage **1**(BF$_4$)$_{12}$ in 0.1 M *n*Bu$_4$NPF$_6$/CH$_3$CN electrolyte at 1000 mV s$^{-1}$. The arrow indicates the direction of the forward scan.

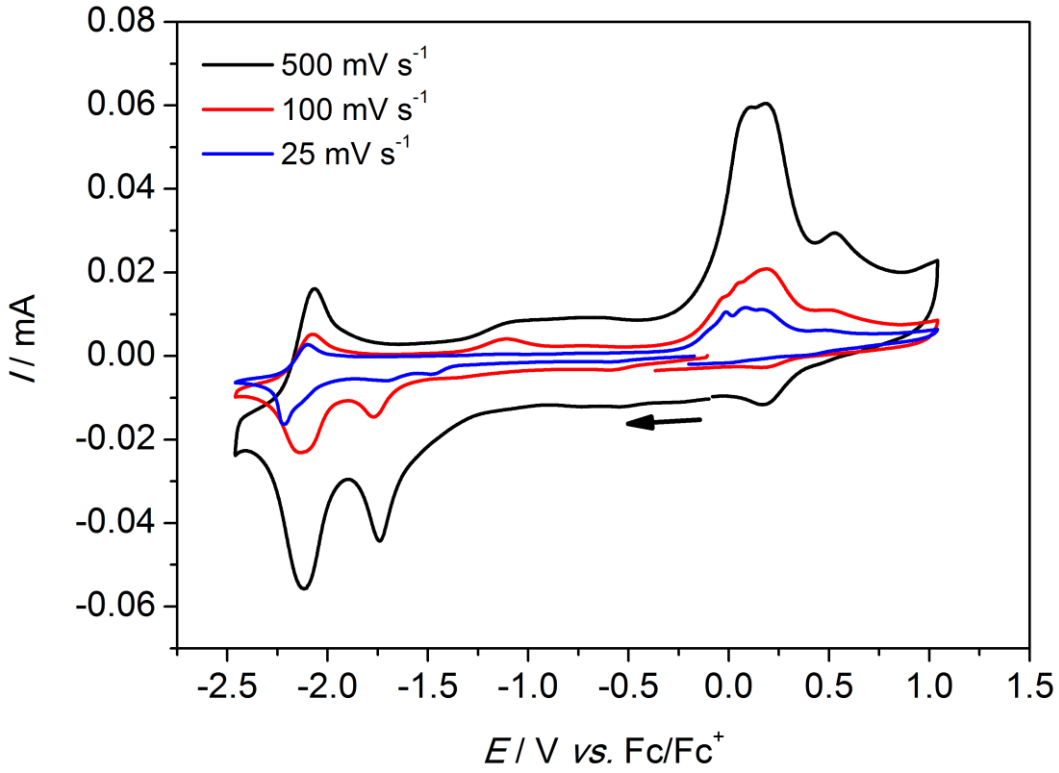


**Figure S36.** CVs of cage **1**$(BF_4)_{12}$ in 0.1 M *n*$Bu_4NPF_6/CH_3CN$ electrolyte at 500, 100 and 25 mV $s^{-1}$, indicating distinct electronic environments of the porphyrin units in **1**. The arrow indicates the direction of the forward scan.

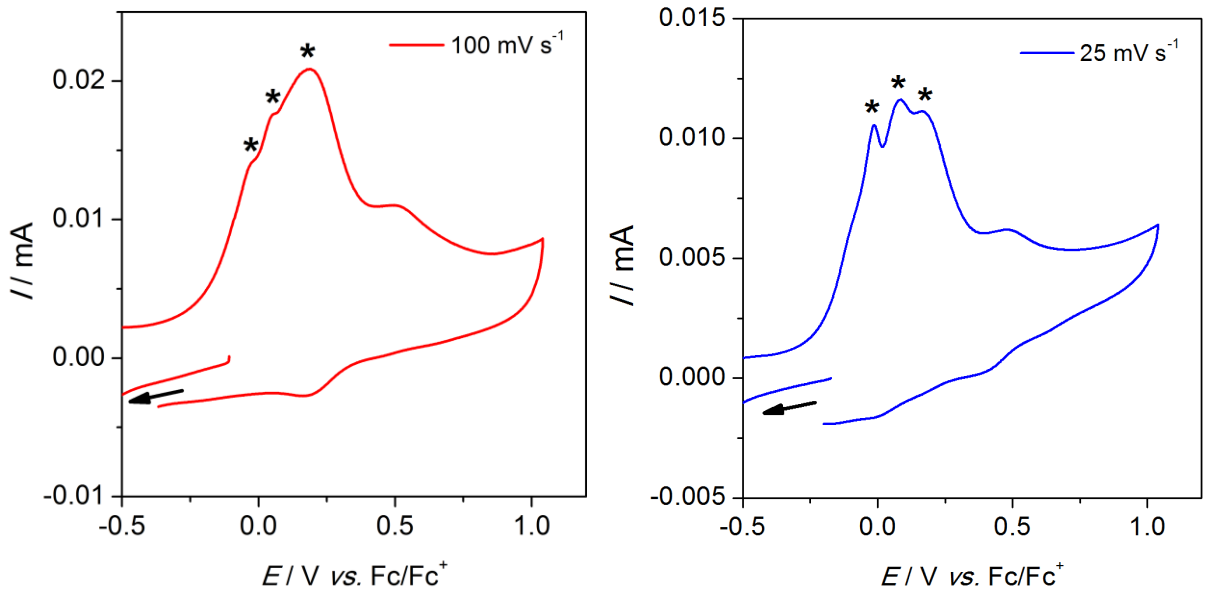


**Figure S37.** Close-ups of anodic sweeps of cage **1**$(BF_4)_{12}$ in 0.1 M *n*-$Bu_4NPF_6/CH_3CN$ electrolyte at 100 (left) and 25 mV $s^{-1}$ (right), showing three distinct waves, consistent with electrical communication between porphyrin units during oxidation. Arrows indicate the direction of the forward scan.

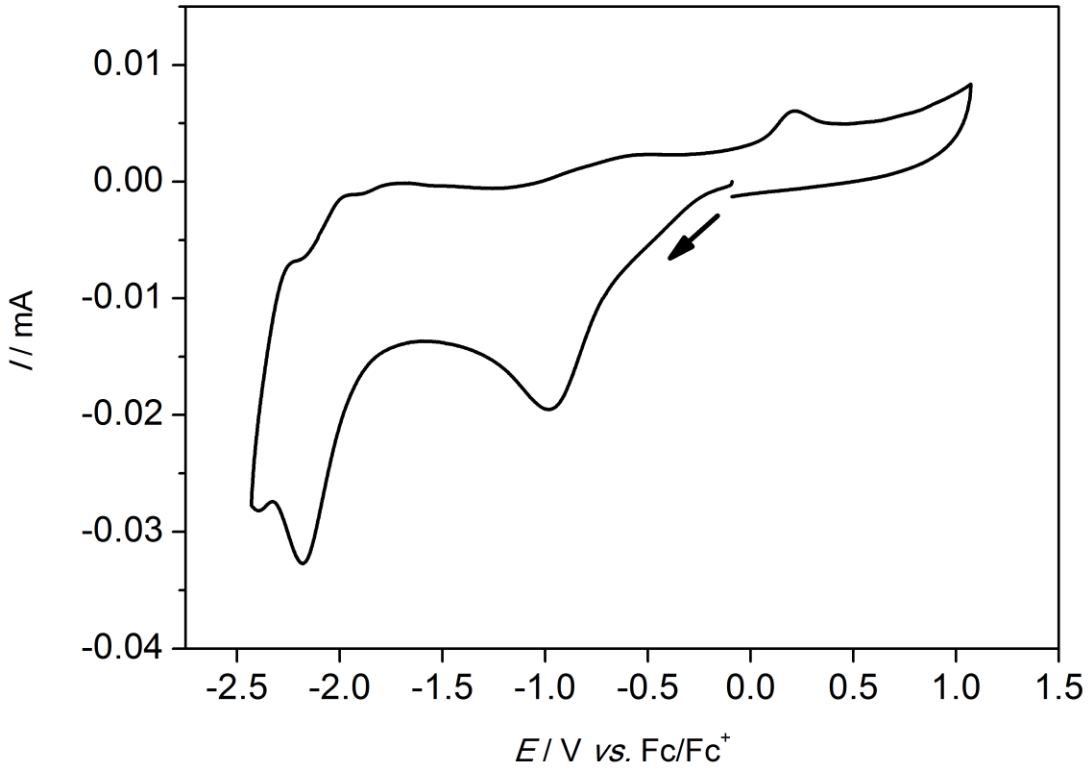


**Figure S38.** CV of $C_{60}$⊂**2** in 0.1 M *n*$Bu_4NPF_6$/$CH_3CN$ electrolyte at 100 mV $s^{-1}$. The arrow indicates the direction of the forward scan.

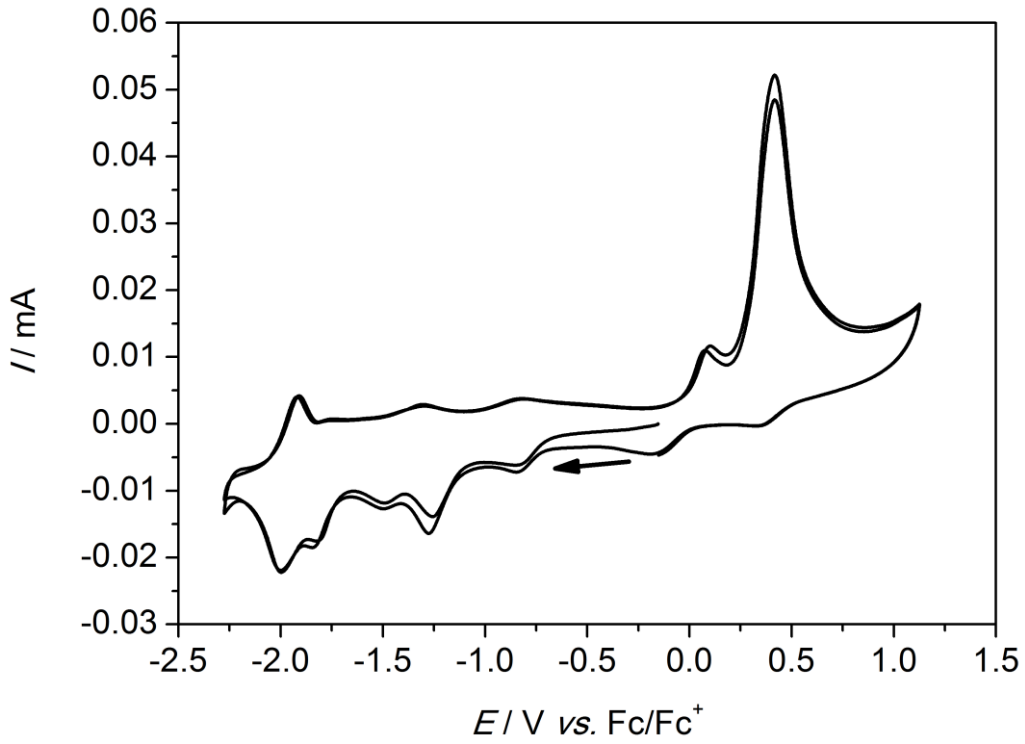


**Figure S39.** CV of $C_{60}$⊂**2** in 0.1 M *n*-$Bu_4NPF_6$/(1:4 DMF:$CH_3CN$) electrolyte at 200 mV $s^{-1}$ over two cycles. The arrow indicates the direction of the forward scan.

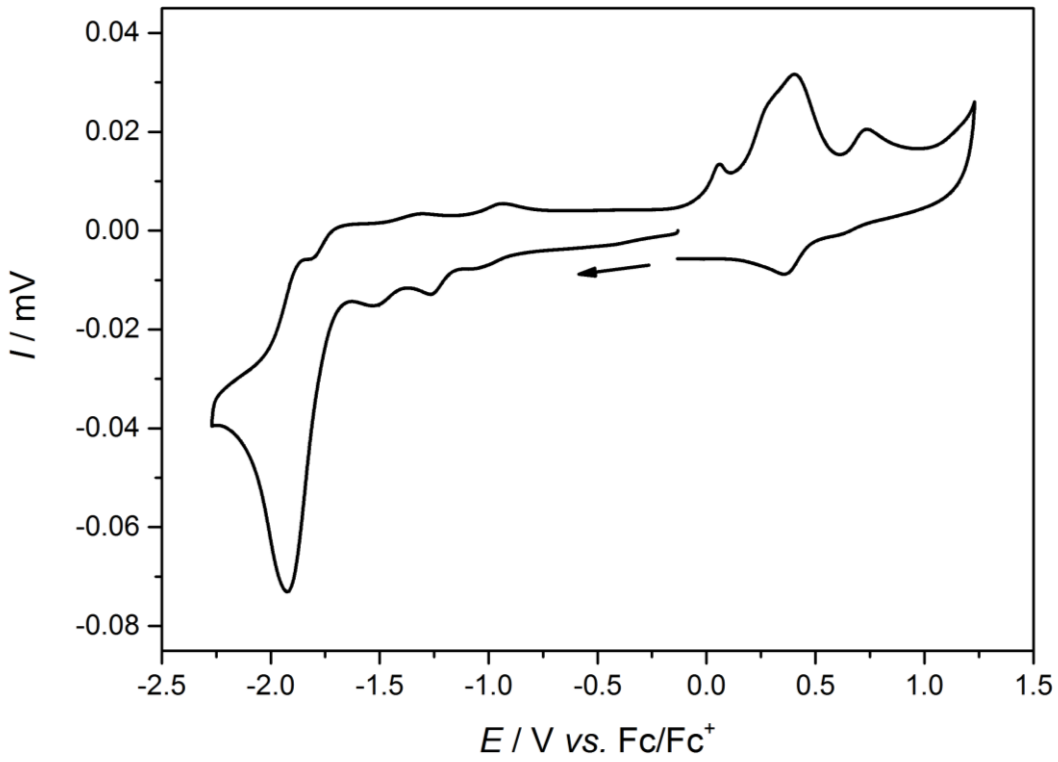


**Figure S40.** CV of $(C_{60})_{1\text{-}3}\subset$**1** in 0.1 M *n*$Bu_4NPF_6/CH_3CN$ electrolyte at 200 mV $s^{-1}$. The arrow indicates the direction of the forward scan.

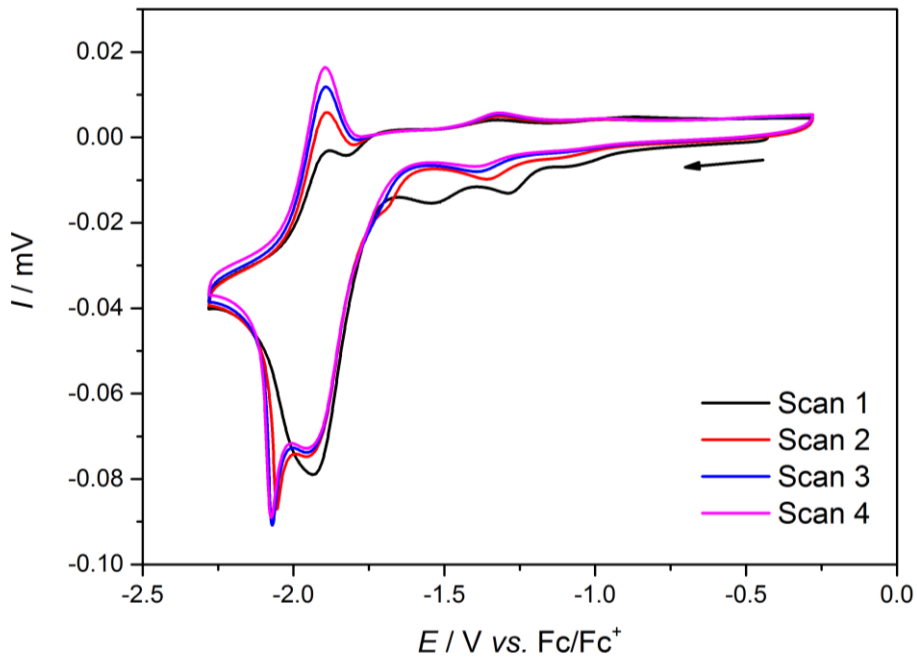


**Figure S41.** CV of $(C_{60})_{1\text{-}3}\subset$**1** in 0.1 M $nBu_4NPF_6/CH_3CN$ electrolyte at 200 mV $s^{-1}$ over 4 sequential cycles. Notable in the voltammogram is the relaxation of redox waves attributed to the bound fullerenes by the second scan, suggesting that the guests are no longer bound in the cage after the first scan. The redox process associated with the porphyrins/pyridyl imines also shifts cathodically following the first scan, resembling that of the free cage (Figure S35) The arrow indicates the direction of the forward scan.

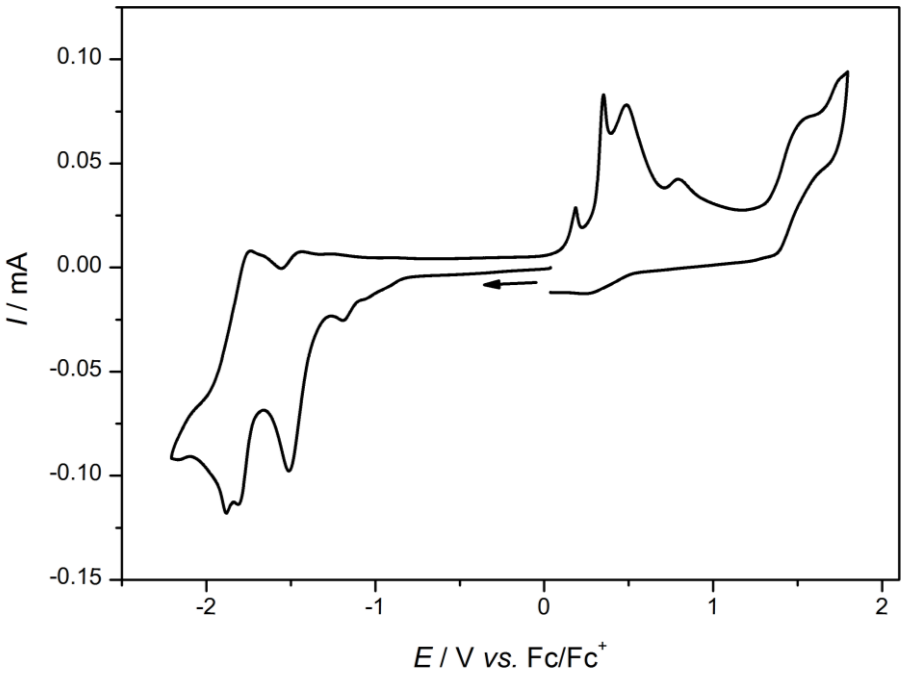


**Figure S42.** CV of $(C_{60})_{1\text{-}4}\subset$**1** in 0.1 M $nBu_4NPF_6/CH_3CN$ electrolyte at 200 mV $s^{-1}$. The arrow indicates the direction of the forward scan. The reduction process associated with the small portion of residual $PhNO_2$ (identified in the NMR spectrum) occurs underneath the wave at –1.5 V.

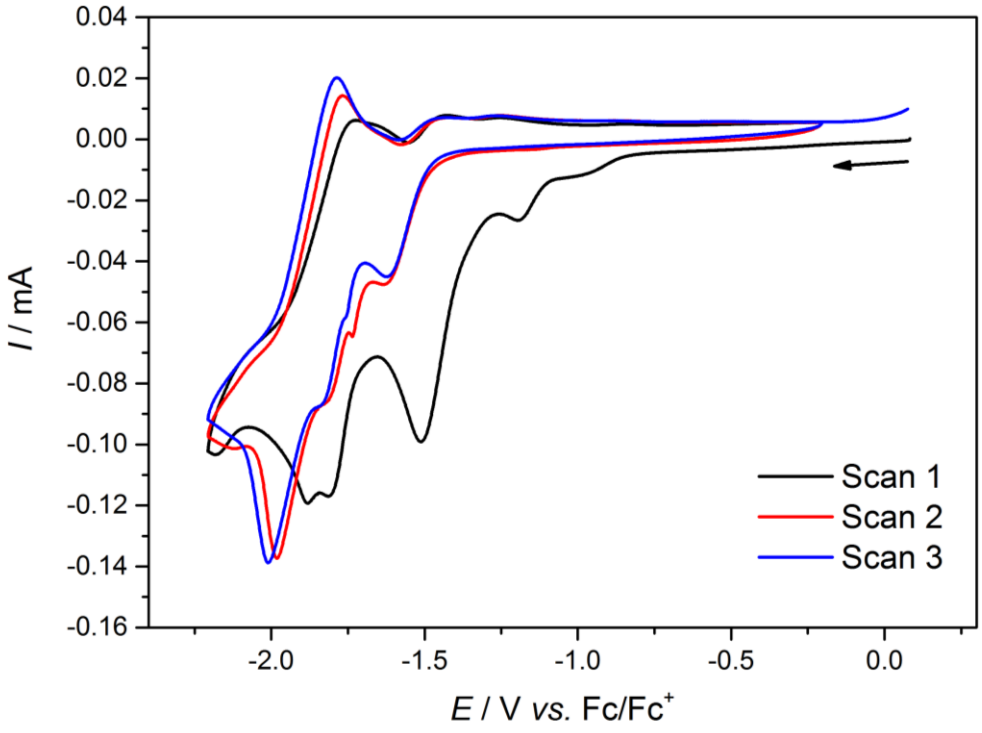


**Figure S43.** CV of $(C_{60})_{1\text{-}4}\subset$**1** in 0.1 M $nBu_4NPF_6/CH_3CN$ electrolyte at 200 mV $s^{-1}$ over three sequential scan cycles. Notable in the voltammogram is the relaxation of redox waves attributed to the bound fullerenes by the second scan, suggesting that the guests are no longer bound in the cage after the first scan. The redox process associated with the porphyrins/pyridyl imines also shifts cathodically following the first scan, resembling that of the free cage (Figure S35). The arrow indicates the direction of the forward scan.

## 9. UV-vis spectra of assemblies in different solvents

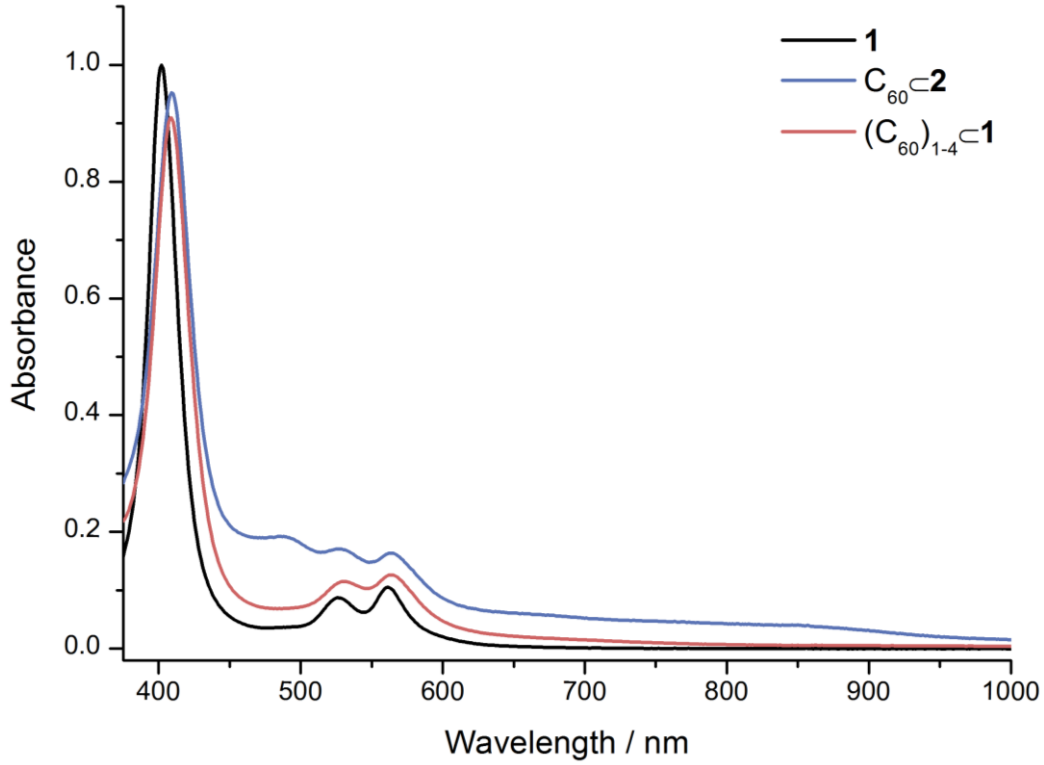


**Figure S44.** UV-vis spectra of assemblies in $MeNO_2$, showing the same features as those recorded in MeCN.

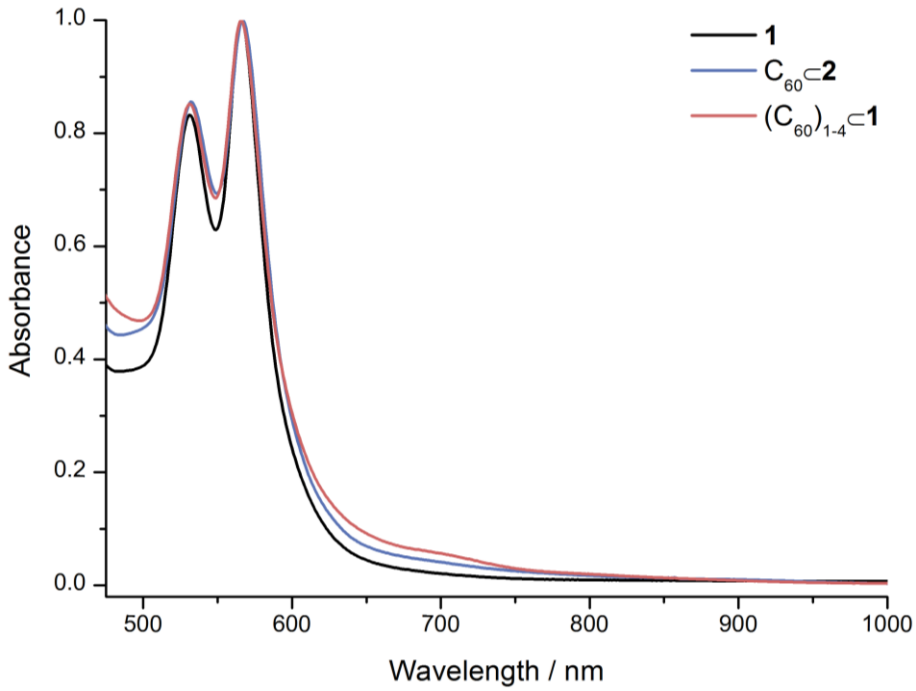


**Figure S45.** UV-vis spectra of assemblies in $PhNO_2$. $PhNO_2$ absorbs strongly at $\lambda < 450$ nm. Weak bands at *ca.* 700 nm are attributed to porphyrin-to-fullerene charge-transfer bands.

## 10. Generation of $C_{60}$ anions within **1** and **2**

### 10.1 Assignment of $C_{60}^{\bullet-}$ or $C_{60}^{2-}$ spectral signatures in MeCN

We hypothesised that the unique electronic environment surrounding the fullerene guests in **1** and **2**, along with the different reduction behaviour observed by CV, would alter the optical properties of their corresponding anions.

Firstly, we attempted to observe free $C_{60}^{\bullet-}$ or $C_{60}^{2-}$ in MeCN; neutral $C_{60}$ is insoluble in MeCN, precluding spectroelectrochemistry in this solvent. Neither $MeNO_2$ nor $PhNO_2$ could be used due to their low reduction potential windows. $C_{60}$ is furthermore highly solvatochromic, necessitating that the comparison of bound $C_{60}^{\bullet-}$ and $C_{60}^{2-}$ to the free anions in the same solvent – MeCN was the only orthogonal choice.

To a solid sample of $C_{60}$ in a UV-vis cuvette was thus added dried and degassed MeCN. The cuvette was sealed under $N_2$, and remained under $N_2$ throughout the experiment. An initial blank spectrum revealed no peaks in the visible or NIR region.

Aliquots of a concentrated solution of $Cp_2Co$ in dry and degassed MeCN were added to the cuvette. Spectra were collected with increasing concentration of $Cp_2Co$ until no insoluble fullerene was observed by eye. The steady evolution of a range of NIR and visible bands was observed (Figure S46).

To determine which bands corresponded to $C_{60}^{\bullet-}$ or $C_{60}^{2-}$, the solution was firstly filtered to remove any insoluble neutral $C_{60}$. The titration of $Cp_2Co$ into this solution was then continued. A steady increase in higher energy near-IR bands at 943 and 826 nm was observed, concomitant with a decrease in lower energy bands at 1072 and 1033 nm (Figure S47). Persistent isosbestic points were observed throughout the titration, indicating conversion of one species to another without degradation. We attribute this to the conversion of $C_{60}^{\bullet-}$ to $C_{60}^{2-}$, as higher redox states lie outside the potential window of $Cp_2Co$ in MeCN (–1.3 V *vs.* $Fc/Fc^+$).[18] NIR bands corresponding to both anions in MeCN were thus assigned as follows.

$C_{60}^{\bullet-}$ = 943 and 826 nm

$C_{60}^{2-}$ = 1072 and 1033 nm

These values correspond well to the electrogenerated fullerene anions reported by Kato at 1073 and 930 nm for $C_{60}^{\bullet-}$, and at 950 and 840 nm for $C_{60}^{2-}$ in $n$$Bu_4NClO_4/CH_2Cl_2$ electrolyte,[19] lending confidence to the assignment of these charged states of $C_{60}$ in MeCN.

Thus, a yardstick for the bands of unbound $C_{60}$ anions was achieved, providing comparison for the ex-*situ* generation of these anions in **1** and **2**.

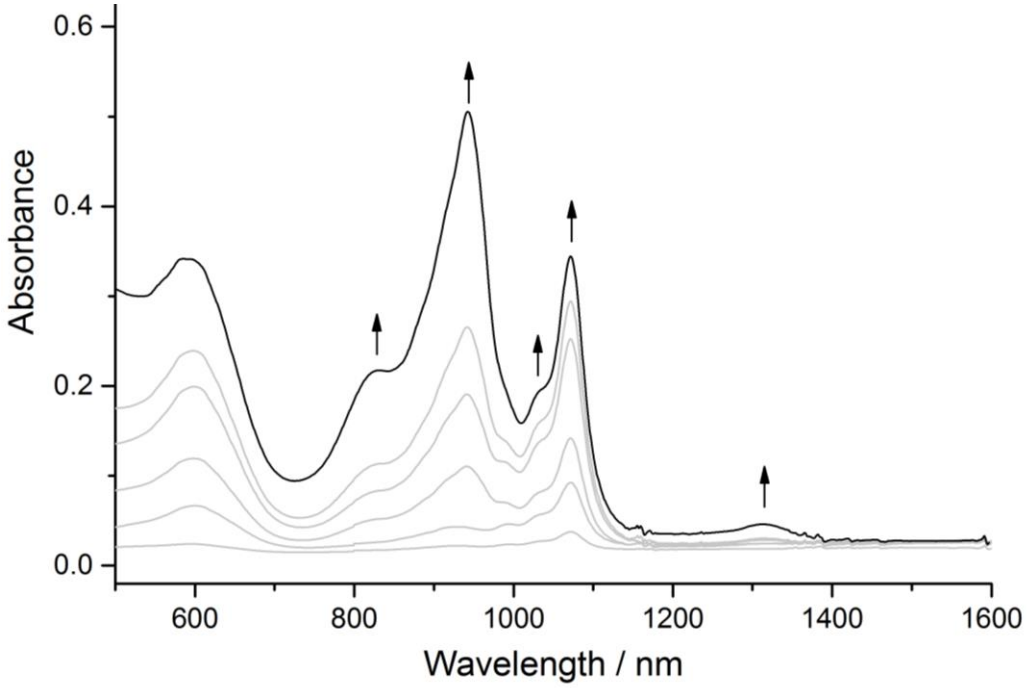


**Figure S46.** The titration of $Cp_2Co$ in MeCN to a solid sample of $C_{60}$ dispersed in MeCN led to the evolution of NIR bands corresponding to anions of $C_{60}$, which were observed to dissolve in MeCN upon *ex-situ* generation.

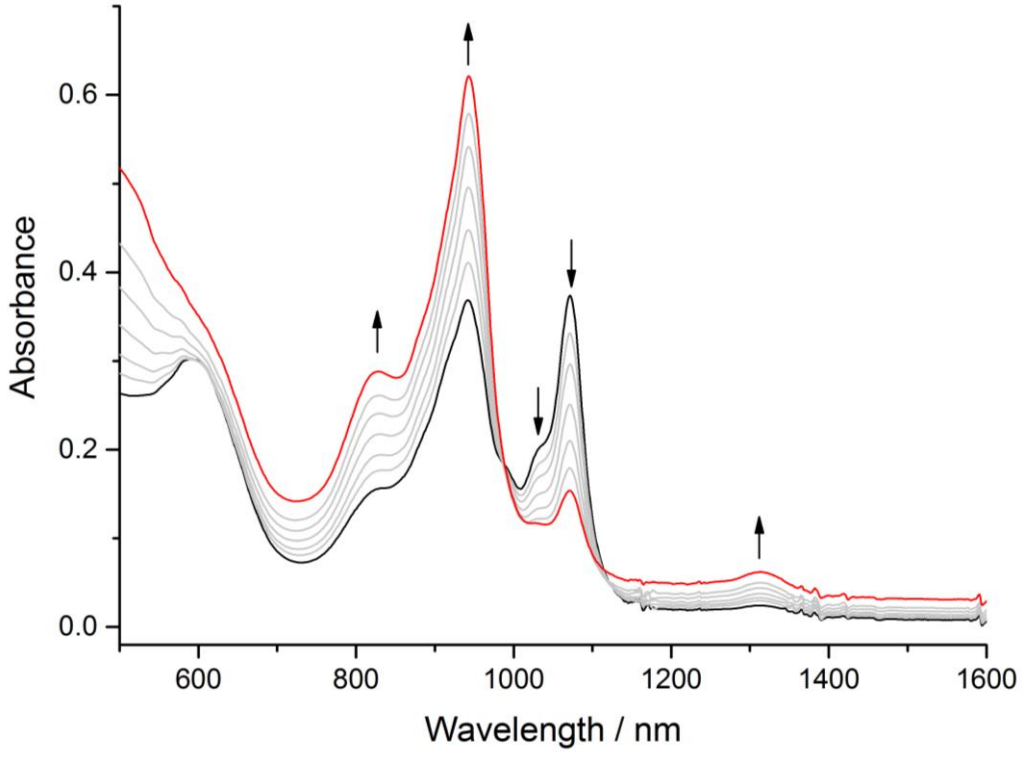


**Figure S47.** After filtering the remaining solid, the continued titration of $Cp_2Co$ in MeCN to the mixture of fullerene anions in MeCN resulted in an increase of higher energy NIR bands at 943 and 826 nm (attributed to $C_{60}^{2-}$), concomitant with a decrease in lower energy bands at 1072 and 1033 nm (attributed to $C_{60}^{\bullet-}$). The persistence of an isosbestic point indicates conversion of one species to another without decomposition.

## 10.2 Generation of $C_{60}^{\bullet-}$ in $(C_{60})_{1\text{-}4}\subset$**1** and $C_{60}\subset$**2**

A sample of $Cp_2Co$ in dried and degassed MeCN was titrated into a sample of either $(C_{60})_{1\text{-}4}\subset$**1** or $C_{60}\subset$**2** in dried and degassed MeCN. Spectral changes occurring in the visible and NIR region were monitored by UV-vis spectroscopy. NIR bands were compared against those of the 'free' anions in MeCN, described in Section 10.1.

$\lambda_{max}$ of $C_{60}^{\bullet-}$ in $(C_{60}^{\bullet-})_x(C_{60})_y\subset$**1** (where $x + y \leq 4$): 1078 nm

$\lambda_{max}$ of $C_{60}^{\bullet-}$ in $(C_{60}^{\bullet-})\subset$**2**: 1083 nm

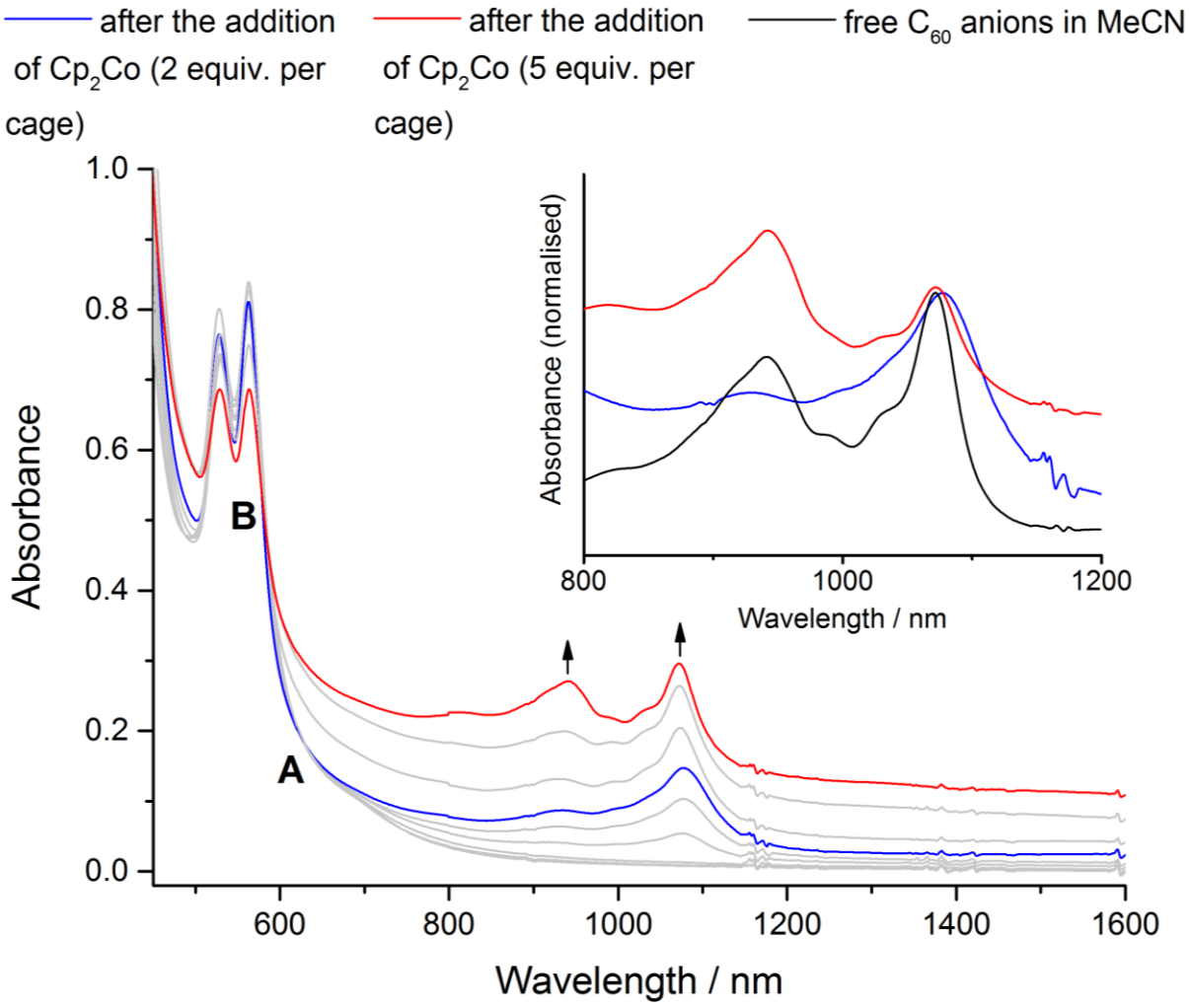


**Figure S48.** The generation of $(C_{60}^{\bullet-})_x(C_{60})_{4-x}\subset$**1** was achieved by the addition of $Cp_2Co$ to a solution of $(C_{60})_{1\text{-}4}\subset$**1** in MeCN. **A** and **B** mark two isosbestic points observed during two stages of the reduction. The inset highlights two important stages in the reduction, wherein a band is observed after the addition of 2 equiv. of $Cp_2Co$ (blue line). This is distinct in broadness and shift compared to the spectrum of $C_{60}$ anions in MeCN alone (black line). During the addition of up to 5 equiv. of $Cp_2Co$ (red line), this band was observed to slowly shift to a wavelength consistent with free $C_{60}^{\bullet-}$ (black line); the appearance of bands corresponding to free $C_{60}^{2-}$ were also observed. We propose that the accessibility of $C_{60}^{2-}$ within the assembly increases the charge repulsion between fullerene units, leading to expulsion from the cage.

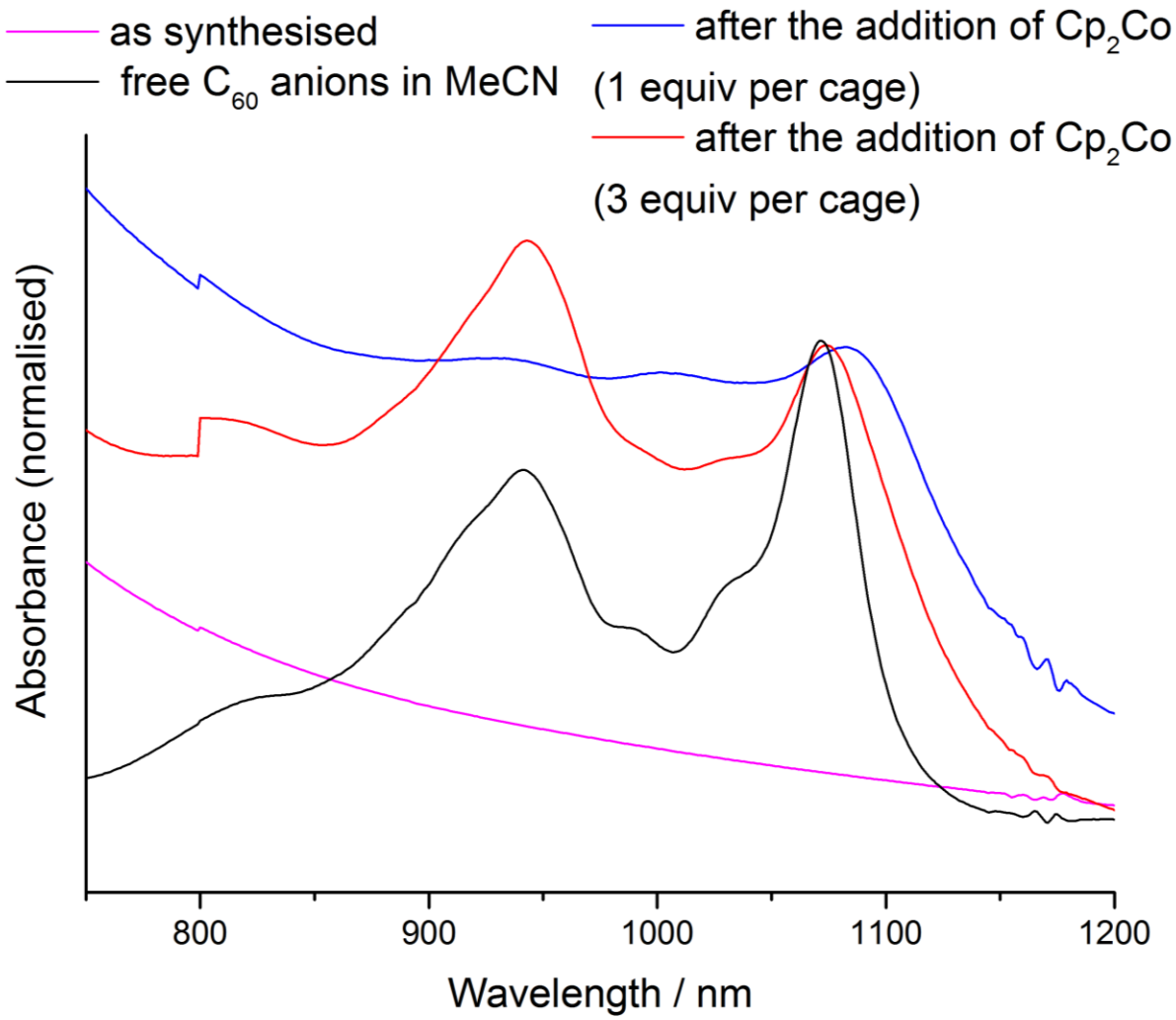


**Figure S49.** The generation of $(C_{60}^{\bullet-})\subset$**2** was achieved by the addition of $Cp_2Co$ to a solution of $C_{60}\subset$**2** in MeCN. Similar to that observed for the reduction of $(C_{60})_{1\text{-}4}\subset$**1**, a band was observed after the addition of 1 equiv. of $Cp_2Co$ (blue line). This is distinct in broadness and shift compared to the spectrum of $C_{60}$ anions in MeCN alone (black line). During the addition of up to 3 equiv. of $Cp_2Co$ (red line), this band was observed to slowly shift to a wavelength consistent with free $C_{60}^{\bullet-}$ (black line); the appearance of bands corresponding to free $C_{60}^{2-}$ were also observed. The complex precipitated upon the further addition of reductant. No definitive isosbestic points were observed over the course of the titration. The above spectra are normalised to allow an easier comparison of the varying $C_{60}^{\bullet-}$ spectra.

## 11. References


1. Wood, D. M., Meng, W., Ronson, T. K., Stefankiewicz, A. R., Sanders, J. K. M., Nitschke, J. R., *Angew. Chem. Int. Ed.* **2015,** *54*, 3988-3992.
2. Berchuck, A., Kamel, A., Whitaker, R., Kerns, B., Olt, G., Kinney, R., Soper, J. T., Dodge, R., Clarke-Pearson, D. L., Marks, P., *Cancer Res* **1990,** *50*.
3. Thordarson, P., *Chem. Soc. Rev.* **2011,** *40*, 1305-1323.
4. Brynn Hibbert, D., Thordarson, P., *Chem. Commun.* **2016,** *52*, 12792-12805.
5. Nowell, H., Barnett, S. A., Christensen, K. E., Teat, S. J., Allan, D. R., *J. Synchrotron Rad.* **2012,** *19*, 435.
6. Bruker-Nonius, *APEX, SAINT and XPREP*. Bruker AXS Inc.: Madison, Wisconsin, USA, 2013.
7. CrysalisPro *CrysAlisPro*, Agilent Technologies Yarton, Oxfordshire, UK, 2009-2016.
8. Farrugia, L. J., *J. Appl. Cryst.* **2012,** *45*, 849-854.
9. Sheldrick, G., *Acta Cryst.* **2008,** *A64*, 112-122.
10. Palatinus, L., Chapuis, G., *J. Appl. Cryst.* **2007,** *40*, 786-790.
11. Hardie, M. J., Torrens, R., Raston, C. L., *Chem. Commun.* **2003**, 1854-1855.
12. Makha, M., Hardie, M. J., Raston, C. L., *Chem. Commun.* **2002**, 1446-1447.
13. Bi, Y., Liao, W., Wang, X., Wang, X., Zhang, H., *Dalton Trans.* **2011,** *40*, 1849-1851.
14. van der Sluis, P., Spek, A. L., *Acta Cryst.* **1990,** *A46*, 194-201.
15. Spek, A. L. *PLATON: A Multipurpose Crystallographic Tool*, Utrecht University: Utrecht, The Netherlands, 2008.
16. N. W. Baxter, P., Lehn, J. M., Rissanen, K., *Chem. Commun.* **1997**, 1323-1324.
17. Hasell, T., Culshaw, J. L., Chong, S. Y., Schmidtmann, M., Little, M. A., Jelfs, K. E., Pyzer-Knapp, E. O., Shepherd, H., Adams, D. J., Day, G. M., Cooper, A. I., *J. Am. Chem. Soc.* **2014,** *136*, 1438-1448.
18. Connelly, N. G., Geiger, W. E., *Chem. Rev.* **1996,** *96*, 877-910.
19. Kato, T., *Laser Chem.* **1994,** *14*, 155-160.